AGU PUBLICATIONS

JGR

Journal of Geophysical Research: Space Physics

RESEARCH ARTICLE
10.1002/2015JA022127

Key Points:
- First report of persistent 3–10 h gravity waves from Antarctic MLT temperatures at McMurdo
- Case study on ~65 h lidar data shows long-lasting waves over 50 h and new wavelet analysis methods
- Statistical study on 5 year June data gives the dominant periods, wavelengths, and frequency spectra

Correspondence to:
X. Chu and C. Chen,
Xinzhao.Chu@Colorado.edu;
cao.chen@colorado.edu

Citation:
Chen, C., X. Chu, J. Zhao, B. R. Roberts, Z. Yu, W. Fong, X. Lu, and J. A. Smith (2016), Lidar observations of persistent gravity waves with periods of 3–10 h in the Antarctic middle and upper atmosphere at McMurdo (77.83°S, 166.67°E), *J. Geophys. Res. Space Physics*, *121*, 1483–1502, doi:10.1002/2015JA022127.

Received 5 NOV 2015
Accepted 29 DEC 2015
Accepted article online 5 JAN 2016
Published online 3 FEB 2016

Lidar observations of persistent gravity waves with periods of 3–10 h in the Antarctic middle and upper atmosphere at McMurdo (77.83°S, 166.67°E)

Cao Chen[1,2], Xinzhao Chu[1,2], Jian Zhao[1,2], Brendan R. Roberts[1,3], Zhibin Yu[1,2], Weichun Fong[1,2], Xian Lu[1], and John A. Smith[1,2]

[1]Cooperative Institute for Research in Environmental Sciences, University of Colorado Boulder, Boulder, Colorado, USA, [2]Department of Aerospace Engineering Sciences, University of Colorado Boulder, Boulder, Colorado, USA, [3]National Ecological Observatory Network, Boulder, Colorado, USA

Abstract Persistent, dominant, and large-amplitude gravity waves with 3–10 h periods and vertical wavelengths ~20–30 km are observed in temperatures from the stratosphere to lower thermosphere with an Fe Boltzmann lidar at McMurdo, Antarctica. These waves exhibit characteristics of inertia-gravity waves in case studies, yet they are extremely persistent and have been present during every lidar observation. We characterize these 3–10 h waves in the mesosphere and lower thermosphere using lidar temperature data in June from 2011 to 2015. A new method is applied to identify the major wave events from every lidar run longer than 12 h. A continuous 65 h lidar run on 28–30 June 2014 exhibits a 7.5 h wave spanning ~60 h, and 6.5 h and 3.4 h waves spanning 40 and 45 h, respectively. Over the course of 5 years, 323 h of data in June reveal that the major wave periods occur in several groups centered from ~3.5 to 7.5 h, with vertical phase speeds of 0.8–2 m/s. These 3–10 h waves possess more than half of the spectral energy for ~93% of the time. A rigorous prewhitening, postcoloring technique is introduced for frequency power spectra investigation. The resulting spectral slopes are unusually steep (−2.7) below ~100 km but gradually become shallower with increasing altitude, reaching about −1.6 at 110 km. Two-dimensional fast Fourier transform spectra confirm that these waves have a uniform dominant vertical wavelength of 20–30 km across periods of 3.5–10 h. These statistical features shed light on the wave source and pave the way for future research.

1. Introduction

Owing to the high-resolution, long-duration, large-altitude-range temperature measurements provided by the Fe Boltzmann lidar at McMurdo [*Chu et al.*, 2011a, 2011b; *Chen et al.*, 2013], a new wave phenomenon in the Antarctic middle and upper atmosphere has been discovered. As illustrated in Figure 1, the raw temperature data from the stratosphere to the lower thermosphere (about 30–115 km) exhibit persistent, dominant, large-amplitude waves with nontidal periods of ~3–10 h and vertical wavelengths of ~20–30 km. Here the word "persistent" is used to describe the fact that these waves continue for a prolonged period, e.g., a single wave event (see section 2) may last at least 10 h, and sometimes over 50 h, in the small field of view (1 mrad) of the lidar beams. If we do not separate the observed wave variations into individual wave events with individual periods, but regard these waves as a group of waves with periods ranging between 3 and 10 h, then this wave group is perpetual. That is, these waves occur on every lidar run, spanning sufficient duration, and occur frequently enough as to appear endless and uninterrupted. There has not been any single lidar run that does not show the signature of this 3–10 h wave group during 5 years of lidar observations at McMurdo, and so far we have not seen any inactive wave gap epoch in observed temperature data. The word "dominant," as used above, is to describe the fact that the temperature variations in the mesosphere and lower thermosphere (MLT) are dominated by these nontidal, short period waves, while the diurnal and semidiurnal tides in temperature are very minimal (up to 1–3 K amplitude) below 100 km [*Fong et al.*, 2014, 2015]. Because planetary waves dominate the temperature variations in the polar winter stratosphere as studied by *Lu et al.* [2013], the 3–10 h waves are not as obvious in the stratosphere as in the MLT (Figure 1). Nevertheless, Figure 2 demonstrates that the 3–10 h waves are still persistent in the stratosphere and mesosphere once planetary waves are filtered out from the Rayleigh temperature perturbations.

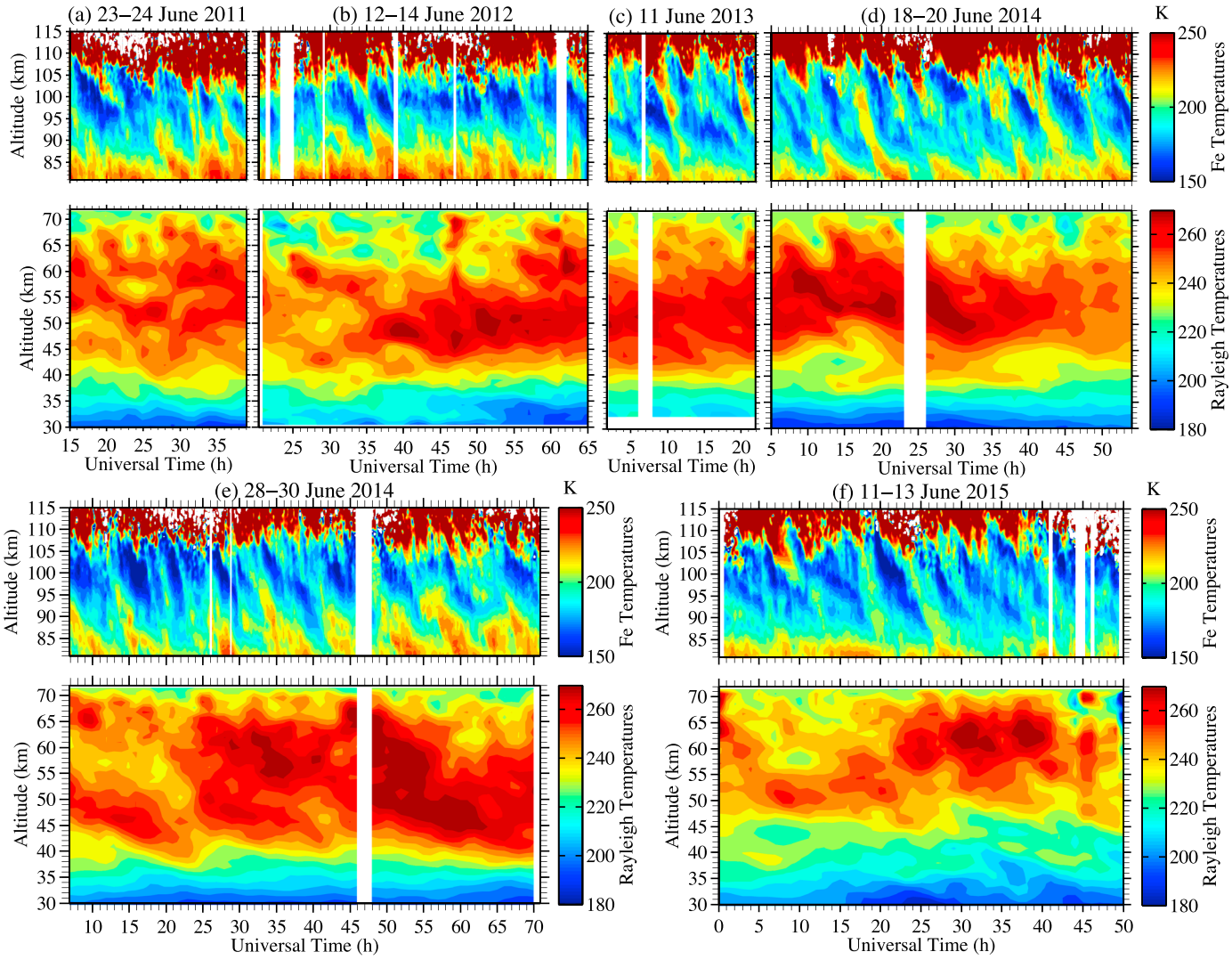

Figure 1. Contours of typical raw temperature observations in June from 2011 to 2015 at McMurdo by an Fe Boltzmann lidar in the MLT region (in the altitude range of 81–115 km) and from Rayleigh integration (in the altitude range of 30–72 km).

These persistent 3–10 h waves were unknown before the McMurdo lidar campaign started providing high-resolution, range-resolved temperature, although observations in the Antarctic middle and upper atmosphere can be traced back to the 1980s or even earlier [*Nomura et al.*, 1987]. Horizontal wind observations using medium frequency (MF) or meteor radars have been used to characterize diurnal and semidiurnal tides [e.g., *Forbes et al.*, 1995; *Baumgaertner et al.*, 2005; *Murphy et al.*, 2006], planetary waves [e.g., *Dowdy*, 2004; *Espy et al.*, 2005], gravity waves [e.g., *Vincent*, 1994; *Hibbins et al.*, 2007], and lamb waves [e.g., *Forbes et al.*, 1999; *Portnyagin et al.*, 2000; *Kovalam and Vincent*, 2003]. However, none of these works noted the persistent 3–10 h waves, except *Forbes et al.* [1999] who described intradiurnal wave oscillations with periods of ~7.5–10.5 h. However, no information was provided on the vertical wavelengths. There have been observational studies of gravity waves, tides, and planetary waves in Antarctica using OH airglow intensities by all-sky imagers [e.g., *Espy et al.*, 2006; *Suzuki et al.*, 2011; *Nielsen et al.*, 2012], wind and temperature measured by Michelson interferometers [e.g., *Sivjee and Walterscheid*, 1994; *Azeem and Sivjee*, 2009], and Fabry-Perot interferometers [e.g., *Hernandez et al.*, 1992; *Wu et al.*, 2005], but these instruments do not have vertical range resolution, and necessarily average over the altitude range of the emission. Na and Fe densities measured by broadband resonance fluorescence lidars were also used to observe wave dynamics in the Antarctic mesopause region [*Nomura et al.*, 1987; *Collins and Gardner*, 1995; *Dietrich et al.*, 2006], but none of them depicted persistent 3–10 h waves. Gravity waves and large-scale global waves such as tides and planetary waves in the Antarctic MLT have also been studied by

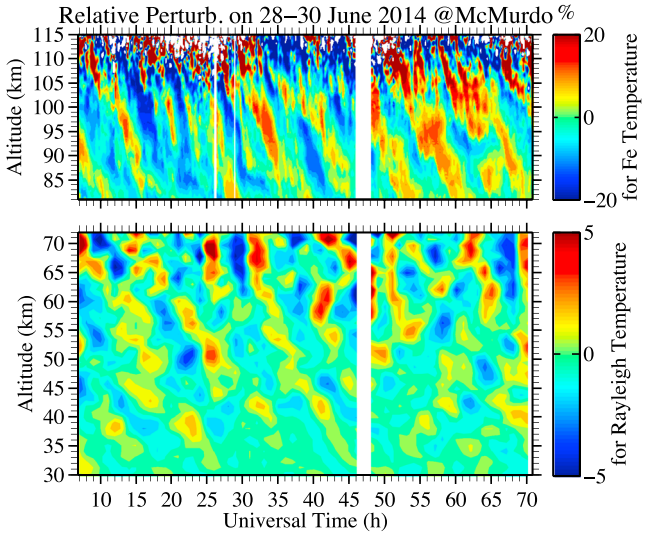

Figure 2. Relative temperature perturbations (unit: %) on 28–30 June 2014 at McMurdo. The Rayleigh temperature perturbations were high-pass filtered with a cutoff frequency of 1/12 h^{-1}, in order to reveal the waves with periods <12 h.

satellite observations [e.g., *Iimura et al.*, 2009; *Morris et al.*, 2009; *McDonald et al.*, 2010]. There are several explanations for the lack of evidence for persistent 3–10 h waves in the observations mentioned above: (1) horizontal winds are usually dominated by tides, thereby obscuring these wave signatures, (2) nonrange-resolved temperature, wind, and airglow data would have easily mistaken these phenomena as tides because no vertical wavelength information was available, and (3) most observations in the past did not have sufficient temporal resolution or time span to reveal these waves deterministically. It is worth mentioning that an Advanced Mesospheric Temperature Mapper operating at the South Pole in the same years as our observations at McMurdo has revealed wave oscillations in the OH layer temperatures with similar periods as the lidar findings (Mike Taylor, Utah State University, private communication).

It is surprising that these waves are so dominant and so strong in range-resolved temperature data, as shown in Figure 1. Temperature perturbations can easily reach ±10–30 K in the mesopause region, but tidal signatures are essentially invisible. This is very different from observations in subpolar, middle- and low-latitude regions wherein tidal signatures usually dominate temperature variations while gravity wave perturbations are relatively minor [e.g., *States and Gardner*, 2000; *She et al.*, 2004; *Chu et al.*, 2005; *Friedman and Chu*, 2007]. *Chen et al.* [2013] conducted a case study for McMurdo waves on 29–30 June 2011, combining the Fe Boltzmann lidar temperature with MF radar horizontal wind data. Although tides are obvious in the winds, 3–10 h waves were found in the range-resolved wind data for the first time. Besides temperature and wind, the 372 and 374 nm Fe density data at McMurdo have also revealed these persistent 3–10 h waves. *Chu et al.* [2011a] presented such a case for summer in January 2011 (see their Figure 4). The downward phase progression in the density data is comparable to that in the temperature data, and interestingly, the cold phase of these waves helps polar mesospheric clouds to form in the summer, as demonstrated in *Chu et al.* [2011a]. A winter case is illustrated in Figure 3. The 3–10 h waves show nicely on the Fe density contours.

There are significant merits of studying these persistent 3–10 h waves. An intriguing question concerns wave sources and the generation mechanisms for such persistent, year-round waves. The waves would have a strong impact on composition and chemistry in the mesopause region because the large temperature perturbations induced by waves can alter the rates of chemical reactions and therefore the concentrations of minor species in the region. Consequently, they are important to the correct modeling of metal layers, polar mesospheric clouds, and other species in the Antarctic middle and upper atmosphere. Because such strong waves cannot continue propagating upward forever, it is important to know where they break and how they impact the upper atmosphere. The implications of these waves on general circulation models and chemical climate models are also significant, particularly with regard to the "cold pole" problem. The cold pole problem refers to the cold bias in modeled winter temperatures in the southern polar stratosphere when

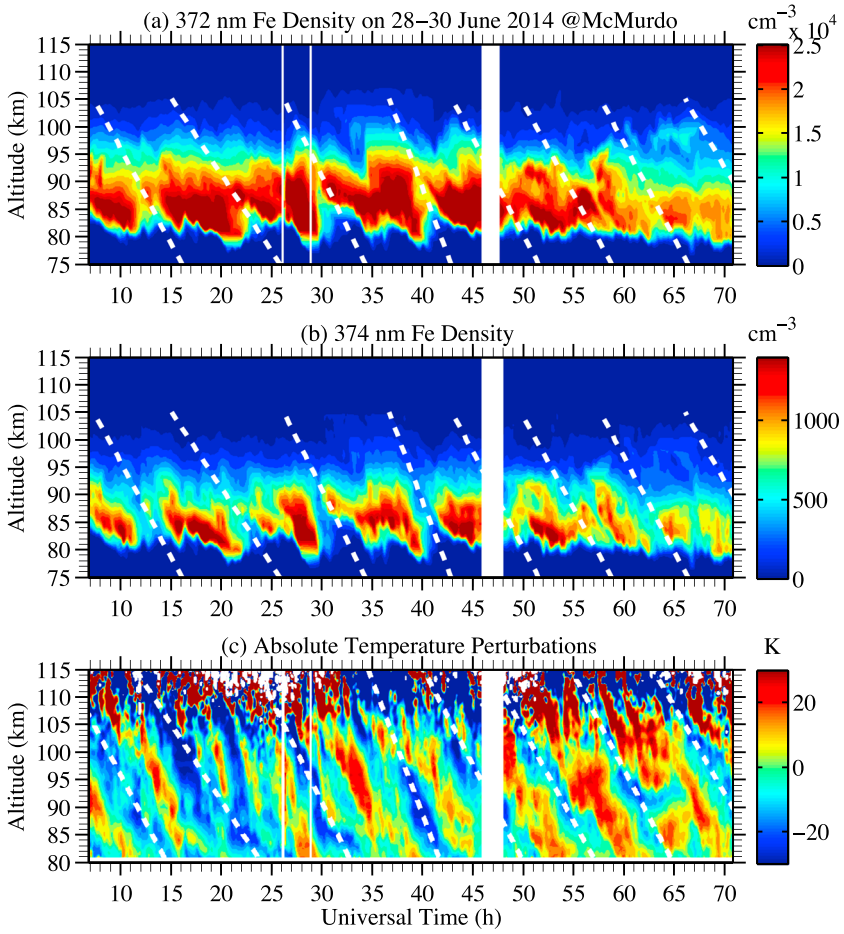

Figure 3. Wintertime Fe densities measured by the (a) 372 and (b) 374 nm channels along with the (c) Fe temperature perturbations (unit: K) in the MLT region on 28–30 June 2014 at McMurdo.

compared to observations [*Garcia and Boville*, 1994; *Eyring et al.*, 2006]. Numerical simulations have indicated missing wave drag in the southern stratosphere as a possible cause. Mountain waves generated by small islands around 60°S [*Alexander et al.*, 2008; *McLandress et al.*, 2012] or inertia-gravity waves (IGWs) [*Tan et al.*, 2011] may provide the missing wave drag. However, the persistent occurrence of 3–10 h waves in the Antarctic mesopause region complicates the picture. If these IGWs survive into the mesopause, then it is unlikely that these waves break or severely dissipate in the stratosphere, so they may not produce sufficient wave drag in the stratosphere. On the other hand, could the unknown sources that persistently generate such waves be responsible for the missing wave drag?

None of the above questions can be answered before these 3–10 h waves are well characterized and documented in the Antarctic middle and upper atmosphere. Therefore, the major goals of this study are to establish the observational fact that the 3–10 h waves are persistent and dominant in the MLT region at McMurdo and to characterize the wave properties using the temperature perturbations. In addition to sophisticated analyses of an individual case demonstrating our new wave analysis methods, we perform a statistical study on the extensive lidar data collected in June through five Antarctic winters from 2011 to 2015. Although these single-location observations cannot resolve the wave nature and source, they do provide the observational basis for future research on answering the important questions listed above.

2. Observations

Since December 2010, the McMurdo lidar observational campaign, conducted by the University of Colorado lidar group, has been in progress for 5 years as of this writing. The upgraded Fe Boltzmann/Rayleigh

temperature lidar [*Chu et al.*, 2002; *Wang et al.*, 2012] has been operated at Arrival Heights observatory (77.83°S, 166.67°E) through a collaborative effort between the United States Antarctic Program (USAP) and Antarctica New Zealand (AntNZ). The observations are year round, weather permitting. Due to the Antarctic darkness, the winter lidar observations experience very low solar background. Combined with a higher Fe layer abundance in winter [*Yu et al.*, 2012], the lidar data in winter months (i.e., May through August) provide the highest resolution and largest range of temperature measurements. Among the winter months, the data quantity is highest in June, primarily due to superior weather conditions. June data have been collected in five consecutive years, from 2011 to 2015. Therefore, this study focuses on the June data analysis, not only because very long data sets can be utilized to inspect wave activity, but also because good statistics can be achieved. These five years of data also allow investigation of year-to-year variability.

Several representative lidar runs are plotted in Figure 1 to illustrate the temperature data quality and length during the month of June. The temperatures in the MLT region (~80–115 km) are derived from the 372 and 374 nm channels of Fe lidar data using the Boltzmann technique [*Gelbwachs*, 1994; *Chu et al.*, 2002], while the temperatures in the mesosphere and stratosphere (~28–73 km) are derived from the Rayleigh scattering obtained by the same Fe lidar with the Rayleigh integration technique [*Hauchecorne and Chanin*, 1980]. Fe temperatures in the MLT are derived with resolutions of 0.25 h and 0.5 km and oversampled to 0.1 h and 0.1 km [*Chu et al.*, 2011b]. The data are then temporally and vertically smoothed with a Hamming window of 0.5 h and 1 km full width at half maximum (FWHM) to further reduce the temperature error. The Rayleigh temperatures have resolutions of 1 h and 1 km and are plotted with steps of 1 h and 1 km. A gap exists between the Fe and Rayleigh temperature regions because the signals obtained from this gap region are too weak to derive reliable temperatures.

Chen et al. [2013] reported two simultaneous inertia-gravity wave events on 29–30 June 2011 at McMurdo, with apparent periods of 7.7 ± 0.2 and 5.0 ± 0.1 h and vertical wavelengths of 22 ± 2 and 23 ± 2 km, respectively. The data on 23–24 June 2011 are shown in Figure 1a, exhibiting similar wave patterns as those in *Chen et al.* [2013]. The case in 2012 covers nearly 2 days, while the case in 2013 is relatively short (~20 h). However, the wave patterns and periods are similar to each other and to the 2011 data. Two long data sets in 2014 are illustrated in Figures 1d and 1e, with ~50 and 65 h of data, respectively. The case in 2015 is again long, covering ~50 h. As mentioned above, weather conditions dictated the data set lengths. Despite the differing lengths of the data sets in each year, the wave patterns, with periods falling between 3 and 10 h, are very similar in each case and similar to many cases that are not shown here. No obvious year-to-year variability is observed, and for this reason, such variability will not be a focus of this study. So far we have not seen any days of data without signatures of such 3–10 h waves. In fact, author Cao Chen was motivated to take nearly 3 days of continuous lidar data in 2014 to investigate whether these waves ever paused. Figures 1 and 2 clearly show that the 3–10 h waves were persistent for three entire days.

The 3–10 h wave signatures also show up clearly in all of the Fe density contours. An example is illustrated in Figure 3, where the Fe densities in 372 nm and 374 nm channels are plotted in direct comparison to the Fe temperatures for 28–30 June 2014. Note the large differences in the absolute Fe densities between two channels. These differences are determined by the Boltzmann distribution of populations on two different energy levels of atomic Fe, in which the 372 nm signals originate from the lowest ground state a^5D_4 and the 374 nm signals originate from a lower excited state a^5D_3. The Boltzmann distribution is temperature-dependent, and therefore, the Fe temperatures are derived from the ratio of the signals from these two channels [*Gelbwachs*, 1994; *Chu et al.*, 2002]. Figure 3 reveals periodic variations of Fe densities in both channels that are consistent with the Fe temperature variations through the 3 days of observations. As illustrated in the figure, eight white, dashed lines are overlaid with the downward-progressing phase lines of the local minimum of Fe density. The density phase lines closely match the cold temperature phase lines, especially when a nearly monochromatic wave dominates. The dashed line at around 20 UT marks a time when multiple waves were present in the Fe temperature contour with no dominant wave. Consequently, this phase line is an average. Although the 374 nm Fe density has the best phase match with Fe temperature, the phase match between the 372 nm Fe density and Fe temperature is reasonable as well. This is consistent with summer observational results by the same lidar at McMurdo (see Figure 4 in *Chu et al.* [2011a]). One implication of this observed phase correlation is that 3–10 h waves may be studied using the 372 nm Fe density data during the summer, when the Fe temperature data and 374 nm Fe density data are of lower quality.

For this study, we will only use the June Fe temperatures for wave analyses because of the very high quality of these data. Since the wind data from the MF radar at Scott Base and Arrival Heights are not available for many days in June, we will focus on the lidar data, conducting a case study in section 3 and then statistical studies in section 4 to characterize the properties and occurrence rate of the 3–10 h waves.

3. Wave Analysis of a Case on 28–30 June 2014

Long, continuous lidar temperature data are essential for understanding these persistent 3–10 h waves. On 28–30 June 2014 (Figure 1e), about 65 h of high-quality lidar data were taken—the longest winter-time observational run in all 5 years of this campaign. By subtracting the data set-mean temperatures at each altitude and dividing by the mean, relative temperature perturbations in the MLT are derived and shown in Figure 2. Note that no filters are applied to the Fe temperature data. The perturbation data provide strong evidence for the persistency of these 3–10 h waves. During nearly 65 h of observations, clear wave structures with a downward phase progression persist in the MLT region, the amplitudes of which can exceed 25 K at 100 km. The temperature variations are dominated by wave oscillations with periods of 3–10 h throughout the observation while diurnal- and semidiurnal-period waves appear minor. In the lower mesosphere and stratosphere, after the long-period (>1 day) waves are high-pass filtered using a sixth-order Butterworth filter with a cutoff frequency of $1/12\,\mathrm{h}^{-1}$, the 3–10 h waves are clearly shown. Several different periods emerge from analysis of the MLT perturbations apparent in Figure 2. We perform detailed wavelet analyses to characterize the properties of each wave packet.

3.1. Wavelet Analysis Method

For separating each wave packet according to its dominant period, amplitude and life span, wavelet analysis is a very effective technique [*Nappo*, 2002]. By decomposing the time series into time-frequency space, wavelet analysis allows us to determine not only the dominant modes of variability but also how those modes evolve with time [*Torrence and Compo*, 1998]. Many studies on gravity waves have used this technique to determine the locations of wave events [e.g., *Sato and Yamada*, 1994; *Zhang et al.*, 2001; *Wang et al.*, 2006; *Lu et al.*, 2015a] and to extract monochromatic wave packets [e.g., *Zink and Vincent*, 2001a, 2001b; *Werner et al.*, 2007; *Murphy et al.*, 2014]. The ability to analyze nonstationary signals gives the wavelet technique advantages over traditional Fourier spectrum analysis, which assumes constant amplitudes of oscillation over the data series.

In this study, we perform a wavelet analysis on the relative temperature perturbations. Since the wavelet transform prefers gap-less data, the original data gap between 46 UT and 48 UT was filled by means of a Lomb-Scargle (LS) periodogram, which is a method first proposed by *Scargle* [1989], and then described in detail by *Hocke and Kämpfer* [2009]. The power spectral density $P(\omega)$, amplitude $A_{FT}(\omega)$, and phase φ_{FT} of the LS periodogram were first calculated from the gapped data series using equations (3)–(10) in *Hocke and Kämpfer* [2009]. Then, the corresponding complex FFT vector $F(\omega)$ was calculated as

$$F(\omega) = A_{\mathrm{FT}}(\omega) exp(i\varphi_{\mathrm{FT}}) \tag{1}$$

An inverse fast Fourier transform was then applied to $F(\omega)$ to provide a nongapped data series. Since the new data series shares the same LS spectrum with the gapped one, this method has the advantage of preserving the spectral features of the original gapped data series [*Hocke and Kämpfer*, 2009].

After the data gap was filled, we then applied a Morlet wavelet transform to the relative temperature perturbations and calculated their amplitude spectra $|W(t, T)|$ as a function of time (t) and period (T) following *Torrence and Compo* [1998]. It is known that wavelet power spectra calculated using the code provided by *Torrence and Compo* [1998] are distorted or biased in favor of large scales or low-frequency oscillations [see *Liu et al.*, 2007]. To overcome the bias of higher amplitudes for longer-period waves, we constructed a new Morlet wavelet function that was modified from $\hat{\psi}(s\omega)$ given by equation (6) and Table 1 in *Torrence and Compo* [1998],

$$\hat{\psi}_{mod}(s\omega) = \left(\frac{\delta t}{2\pi^{1/2} s}\right)^{1/2} \hat{\psi}(s\omega) = H(\omega) e^{-(s\omega-\omega_0)^2/2} \tag{2}$$

where s is the wavelet scale, which is almost equivalent to period T [*Torrence and Compo*, 1998]; δt is the data sample interval; ω_0 is the nondimentional frequency, which is taken to be 6 [*Torrence and Compo*, 1998]; and

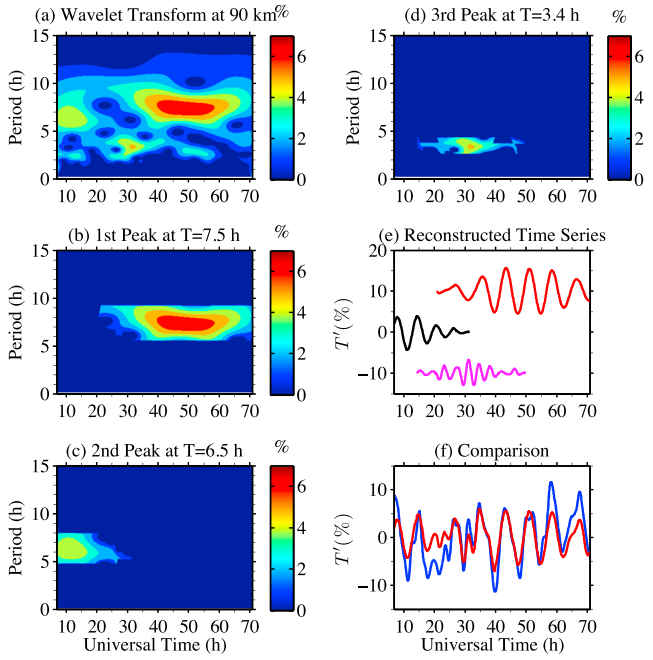

Figure 4. Example of the Morlet wavelet amplitude spectra of relative temperature perturbations at 90 km obtained on 28–30 June 2014 and extractions of wave packets. (a) Amplitude of wavelet spectrum. (b–d) Three identified peaks (at ~7.5, ~6.5, and ~3.4 h) and their extensions in the wavelet amplitude spectrum. (e) Reconstructed relative perturbations from each peak extensions around ~7.5 h (red), ~6.5 h (black), and ~3.4 h (magenta). Each line plot is offset by 10%. (f) Comparison between the sum of three reconstructed perturbations (red) and the original temperature perturbation (blue).

$H(\omega)$ is the Heaviside step function: $H(\omega) = 1$ if $\omega > 0$, $H(\omega) = 0$ otherwise. Using this "corrected" wavelet function, our forward-modeling tests show that the amplitude of the wavelet transform no longer biases toward the longer period features. This correction is very important for our purpose because it will prevent any bias toward the larger-scale oscillations when extracting the dominant waves. Two more advantages of this corrected wavelet function are as follows: First, the wavelet amplitude does not depend on the resolution of the data (δt) because δt has been canceled out in equation (2). This resolution independency allows comparison of the wavelet amplitude between data sets with different resolutions. Second, the wavelet amplitude is equivalent to the amplitude given by Fourier transform. Essentially, the new wavelet transform can give an accurate estimate of the wave amplitude. As an example, the wavelet amplitude spectra of the temperature relative perturbation time series at 90 km on 28–30 June 2014 are shown in Figure 4a. Several peaks are clearly shown: a dominant one with a period of 7.5 h and another two with periods of 6.5 h and 3.4 h. The value of each peak in the spectrum correctly represents the peak amplitude of each corresponding oscillation. The peak amplitude of the 7.5 h wave is 7.0%, while the peak amplitude of the 6.5 h and 3.4 h waves are 4.8% and 5.0%, respectively. It also demonstrates that the 6.5 h wave dominates in the first ~10 h of the temperature measurements, after which the 3.4 h wave dominates for the next ~20 h and the 7.5 h wave becomes dominant for the remainder of the temperature measurements. This result agrees with the observations in Figure 2.

To extract the perturbations induced by individual waves and characterize their wave parameters, we first search for local maxima $|W(t_{max}, T_{max})|$ in the amplitude spectrum. Then, for each of these maxima, we scan the surface of $|W(t, T)|$ around (t_{max}, T_{max}) to identify an extended region about the peak. This extended region about the peak is defined as the region in which the amplitude $|W(t,T)|$ monotonically descends from $|W(t_{max}, T_{max})|$ to where the amplitude either drops below a threshold (W_{th}) or begins to increase. For this study, we define a threshold of $W_{th} = 2\%$. Using this method, the major peaks at periods T~7.5 h, T~6.5 h, and T~3.4 h and their corresponding extensions were identified in the wavelet amplitude spectrum, as shown in Figures 4b–4d. Then, the complex wavelet transform coefficients ($W(t_n,T_j)$) within each peak extension

were recorded and reconstructed back to the time domain by summing the real part of the wavelet transform over all scales [*Torrence and Compo*, 1998]:

$$x_n = \frac{\delta j \delta t^{1/2}}{C_\delta \pi^{-1/4}} \sum_j \frac{\Re\{W(t_n, s_j)\}}{s_j^{1/2}}, \tag{3}$$

where x_n is the reconstructed time series at t_n, $C_\delta = 0.776$ for Morlet ($\omega_0 = 6$), and δj represents the sampling spacing of the scales. The reconstructed, relative temperature perturbations from each wavelet peak extension are shown in Figure 4e. As can be seen, each reconstructed time series is quasi-monochromatic, and their peak amplitudes agree well with the wavelet spectra. Another feature of the reconstructed time series is that they have wave packet-like shapes in the time domain, which matches a character of gravity waves, i.e., being intermittent. This will be further discussed in section 4.1. Finally, in order to further validate this method, these three reconstructed time series are summed to compare with the original data in Figure 4f. The results show good agreement with the original time series in general, and better agreement can be achieved if more peak extensions are included in the reconstruction (not shown here). These extra peak extensions include the 10.6 h wave shown in Figures 4a and 5e and waves with periods longer than 15 h not shown in Figure 4a.

3.2. Periods and Life Span of Five Wave Events

The above method can only be used to extract wave packets from a 1-D time series. However, since atmospheric waves propagate in both time and space, we need to extract the dominant waves in the 2-D (both time and altitude) domain. In order to do this, 1-D wave packets with similar periods (within ±0.5 h), but detected at different altitudes, are grouped into one 2-D wave packet. For each lidar observation, we can extract several dominant 2-D wave packets, each of which is called a "wave event." Only the wave events with vertical coverage larger than 4 km were selected for future analysis. We make this selection for the following two reasons. First, oscillations with no vertical coherence, perhaps due to noise or false detection by the wavelet transform, will be excluded from the analysis. This spatial scrutiny ensures that each wave event is a real atmospheric wave that travels in both time and space. Second, the spatial examination also helps us to study how wave characteristics change in a relatively large range of altitudes.

Using the above method, five wave events are identified for the ~65 h lidar run during 28–30 June 2014 and the extracted 2-D perturbations are shown in Figure 5. The mean period of each wave event is obtained by averaging the peak periods over the height range where the event is present. These five wave events have mean periods of T~7.5 h, T~6.5 h, T~3.4 h, T~10.6 h, and T~3.9 h, respectively. Each wave event shows coherent, downward phase lines and a consistent period across altitude—the characteristics of quasi-monochromatic gravity waves. These wave events all show "come-and-go" features (with a wave packet -like "envelope" of amplitudes), instead of constant amplitudes. Their occurrences also overlap with each other. As stated in section 1, if we regard these wave events as a group of waves with periods ranging between 3 and 10 h, then this wave group is perpetual. The total life span of each major wave event is defined as the span from the start of the appearance of the wave at any altitude until the last disappearance of the wave at any altitude. The results for the life spans of five wave events during this case are shown in Figure 6. The wave packet of period T~7.5 h is the most persistent wave event, and its life span is nearly 60 h in our observation, ~90% of the entire observation period. The other dominant wave events also last long ($>$30 h).

The presence of such persistent and long duration waves in the lidar data is astonishing. We may be able to make several inferences from this. Either the horizontal wavelengths of the waves are very long, or the sources producing these 3–10 h waves are persistent, or both. Future searches for wave sources should keep this observational fact in mind. Another interesting result is that four waves with periods of 7.5, 6.5, 3.4, and 10.6 h occur simultaneously around 20–30 UT in Figure 4a with comparable wave amplitudes. This explains why the second white dashed line from the left in Figure 3 does not follow any single wave but is an average over multiple waves.

3.3. Phase, Vertical Wavelength, and Vertical Phase Speed

Phases and vertical wavelengths are important for understanding the nature of waves. For example, if the waves are of tidal origin then they should have a relatively fixed phase. If the waves are normal modes, their vertical wavelengths may be very long. After wave events were identified, we derived phases and vertical wavelengths for each wave event using the method described by *Chu et al.* [2011b]. The mean phase is

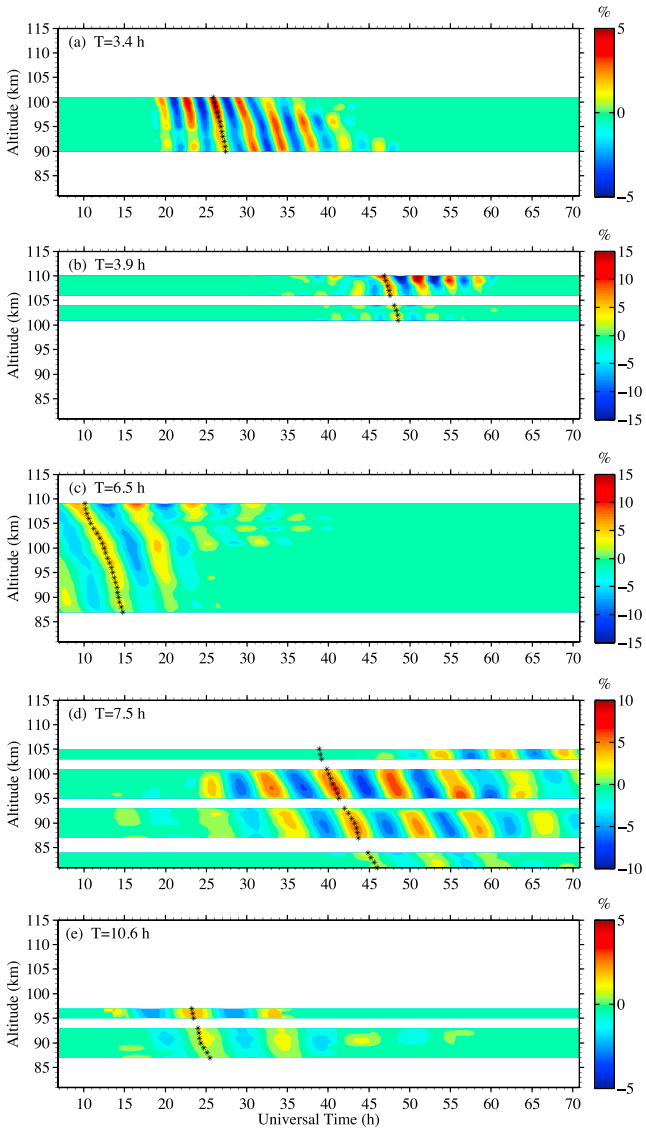

Figure 5. Wavelet reconstructed relative temperature perturbations of five wave events with periods of (a) 3.4 h, (b) 3.9 h, (c) 6.5 h, (d) 7.5 h, and (e) 10.6 h during 28–30 June 2014. Black asterisks on each contour plot mark the derived average hot phase line for each wave event.

defined as the universal time of maximum temperature perturbation, and the derived phase profile for each wave event is plotted on each contour in Figure 5 as black asterisks. The same phase profile, modulo 24 h, is shown in Figure 7a. The derived phases are quite smooth with the obvious downward progression. The phases of the five events occur at different local/universal times.

The vertical wavelength λ_z is derived as below

$$\lambda_z = T/(d\Phi/dz) \tag{4}$$

where T is the wave period, Φ is the phase expressed in universal time, and z is the altitude. Even though the periods of individual wave events are quite different, the vertical wavelengths, as shown in Figure 7b, are mostly between 20 and 30 km, except at lower altitudes for the 6.5 h and 10.6 h waves. It appears that the 3–10 h waves in the MLT region exhibit a preference in vertical wavelength of 20–30 km. Such a result is surprising as we are not aware of any mechanisms that would limit, or select for, vertical wavelengths in the MLT region. The vertical phase speed (c_z) profiles derived from the wavelet analyses are shown in Figure 7c. The observed c_z of each wave is mostly around 1 m/s, comparable to the two IGWs studied by *Chen et al.* [2013], in

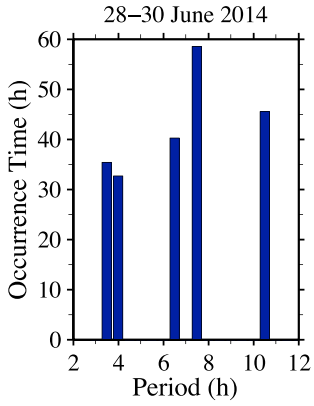

Figure 6. Life spans (in hours) of five wave packets identified from the wavelet analysis are plotted against their observed periods for 28–30 June 2014.

which $c_z = 0.8$ m/s and $c_z = 1.2$ m/s for the 7.7 h and 5 h waves, respectively. This common c_z is also comparable to the summer case reported in *Chu et al.* [2011a], where the downward phase speed is ~0.7 m/s. We did not find any obvious or consistent trends in the c_z variations with altitude.

4. Statistical Studies of Wave Characteristics in June

Although several case studies have identified the 3–10 h waves as IGWs [*Chen et al.*, 2012, 2013], case studies cannot provide an estimate on the occurrence frequency or representativeness of particular cases, and the results could be biased by sample selections. Moreover, it is quite difficult to make comparisons of case study results with other data sets, such as observations using different instruments at different locations and time, and with assimilated or forecast model data. Therefore, a statistical study is crucial to establish an observational basis of the properties of these 3–10 h waves that would serve as a foundation for future studies. In this section, the temperature data in June from 2011 to 2015 are used to derive several statistical wave properties. We select observation episodes longer than 12 h for the study because this allows us to accurately determine the wave periods. A total of ~323 h of data are used in this study, and a list of the data is given in Table 1.

4.1. Statistical Results

Applying the same wave analysis technique as that described in section 3 to the 5 years of June data, we identify a total of 35 wave events. Periods, life spans, phases, vertical wavelengths, and phase speeds are calculated and recorded for all these wave events. We then categorize each wave event by its period. The proportion of time spans for identified wave events as a fraction of the complete observation time, plotted against the wave period, is shown in the histogram (Figure 8a). Figure 8a suggests that waves with periods of ~3.5, 5, 6, 6.5, and 7.5 h have the highest occurrence frequency, each occurring ~25–30% of the time in 323 h data examined. If we do not separate each wave event, but treat all of them as a group, the 3–10 h waves can be considered persistent. The percentage of the spectral power between periods of 3–10 h over the total spectral power was calculated. Then, the total time that this percentage exceeds 50% was counted. The results for altitudes from 80 to 110 km are shown in Figure 8b. Between 80 and 110 km, the 3–10 h waves have more than half of the entire spectral power for ~93% of the time. This result confirms our intuition that these waves are persistent and dominant and exhibit long lifetimes.

It is worth pointing out that the persistence of these 3–10 h waves does not contradict a consensus that gravity waves are inherently intermittent. In the wave dynamics field, waves are considered to be intermittent when the amplitude of wave-induced disturbances is not constant, but varies with time scales comparable

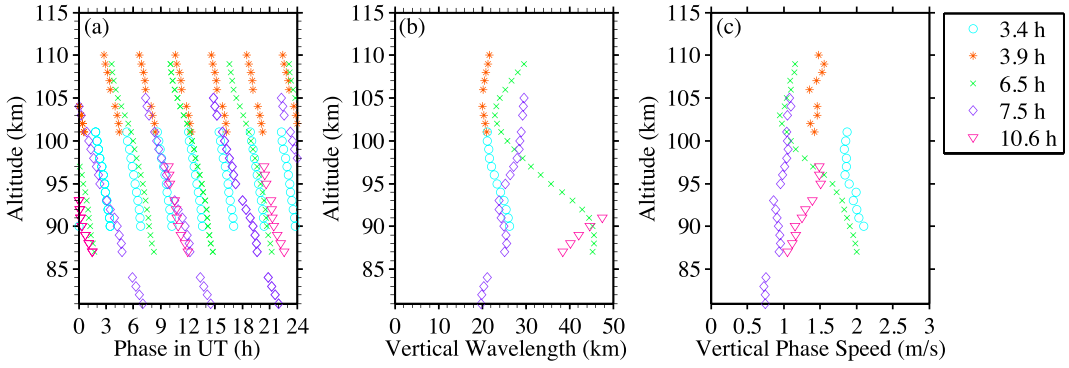

Figure 7. Vertical profiles of (a) derived phase, (b) vertical wavelength, and (c) vertical phase speed for each wave event on 28–30 June 2014. Results for each event are denoted in different colors and markers as indicated in the legend.

Table 1. Number of Observations and Hours of June Data Used in the Analysis

Year	2011	2012	2013	2014	2015
Number of observations	3	1	1	3	3
Hours	63	31.5	20.3	134.5	73.9

to those of the wave packets [*Hertzog et al.*, 2012]. Many observational studies have shown that gravity waves are generally observed as wave packets [e.g., *Pfister et al.*, 1993; *Alexander and Pfister*, 1995; *Eckermann and Preusse*, 1999; *Plougonven et al.*, 2008]. This wave packet behavior implies that the amplitudes of gravity waves vary in time and space, and that therefore, by nature, gravity waves are inherently (at least to some extent) intermittent [see *Fritts*, 1984; *Nappo*, 2002; *Vadas*, 2005; *Vadas and Fritts*, 2006; *Alexander et al.*, 2010; *Hertzog et al.*, 2012]. This concept of intermittency is not in opposition to the definition of persistency in our analyses. Here the persistency ignores variations in wave amplitude over time. In fact, our wavelet analysis and reconstruction have shown these waves to exhibit a packet-like shape in the time domain (see Figures 4 and 5 as examples), suggesting that the highly persistent 3–10 h waves we observed are intermittent as well.

For each wave event, profiles of wave phases (defined as the UT time when the maximum temperature perturbations occur at each altitude), vertical wavelengths, and vertical phase speeds are derived using the method described in section 3.3. The wave phase modulo the corresponding wave period at each altitude is calculated and shown for 5 years of data in Figure 9a. The phases are categorized in three different groups, i.e., 3–5 h, 5–7 h, and 7–10 h, based on their mean wave period, and are denoted in three different colors in order to show if there is any consistency within each group. These three groups of waves are chosen because their periods are close to some harmonics of Earth's rotational period (4, 6, and 8 h), which are also tidal wave periods. As can be seen from the figure, all of the extracted wave phases show a downward phase progression. Within each group, wave phases at each altitude are random. Figures 9b and 9c show the derived λ_z and c_z profiles, respectively. Even though the periods of the wave events are quite different, the vertical wavelengths λ_z remain around 20–30 km, while the vertical phase speeds c_z remain around 0.8–2 m/s. Both λ_z and c_z profiles do not exhibit any obvious dependence on altitude, but are rather uniform throughout the MLT region. These statistical studies on the 3–10 h waves illustrate the randomness of the phases, yet uniform vertical wavelengths and phase speeds. Such information will be useful in studies of the nature of the waves and their possible sources.

4.2. Frequency Power Spectra and 2-D Wave Spectra of the MLT Temperatures

Even though there are numerous lidar studies on frequency power spectra in the MLT region based on Na densities [*Senft and Gardner*, 1991; *Beatty et al.*, 1992; *Senft et al.*, 1993; *Collins et al.*, 1994, 1996; *Yang et al.*, 2006], there

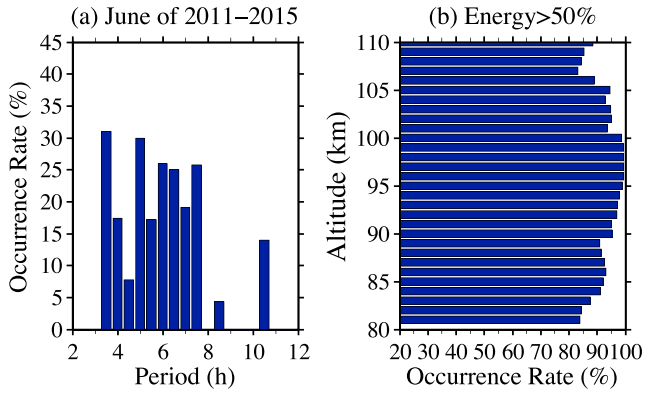

Figure 8. (a) Ratio of time span of a wave event over entire observation time (323.2 h) plotted against the wave period in June from 2011 to 2015. Each bin is 0.5 h wide. (b) Ratio of the time length over entire observation length when the spectral energy of the 3–10 h waves exceeds 50% of the total spectral energy. The results at different altitudes were shown. Each bin is 1 km wide.

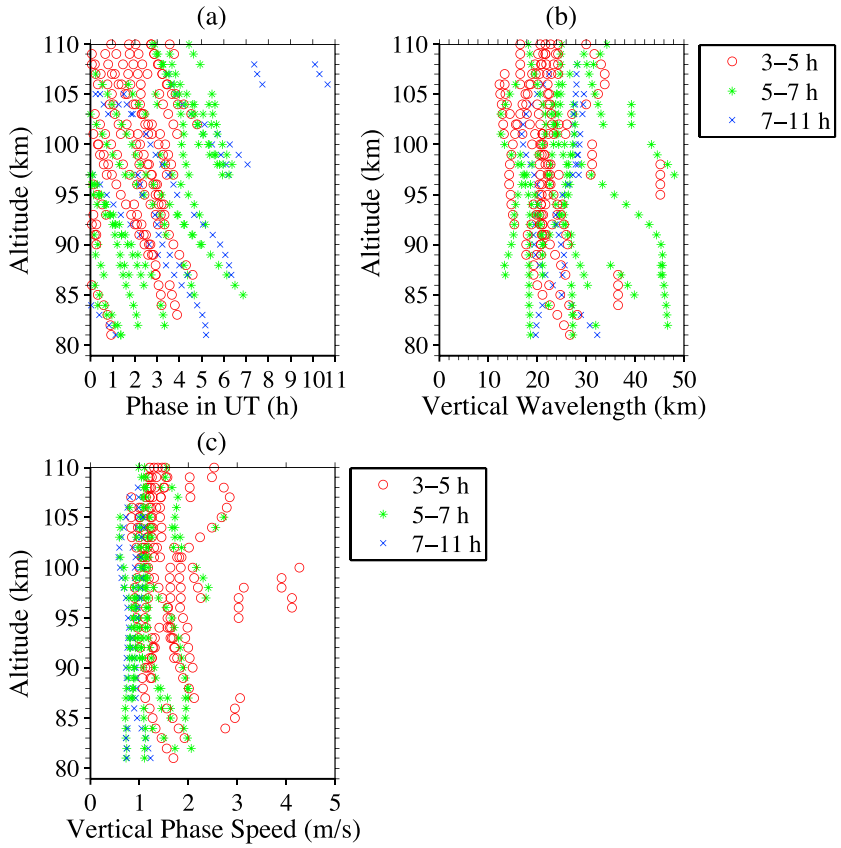

Figure 9. Vertical profiles of (a) phase, (b) vertical wavelength, and (c) vertical phase speed for each wave event in June from 2011 to 2015. The results are categorized in three different groups, i.e., 3–5 h, 5–7 h, and 7–10 h, based on their mean wave periods, and are denoted in three different colors.

are few studies based on temperature data in this region. One study that covers such a topic was performed by *Gardner and Yang* [1998] based on 65 h (eight nights) of observations at a midlatitude site in New Mexico. However, no information was given on how the spectra change with height and the length of each observation limited their study. To calculate the power spectral density (PSD), we first derive the relative temperature perturbations from raw temperature data. Then, for each episode, the PSD is calculated at each altitude using a prewhitening and postcoloring method. This method has been widely used and has been shown to reduce sidelobe leakage from the finite length of the rectangular window [e.g., *Tsuda et al.*, 1990; *Nakamura et al.*, 1993; *Allen and Vincent*, 1995; *Dewan and Grossbard*, 2000; *Yang et al.*, 2010]. However, all of the above studies have used the first-order autoregressive (AR) model (first-order differencing) with a fixed coefficient of $\varphi = 0.95$ or $\varphi = 1$. Among them, *Dewan and Grossbard* [2000] found the first-order AR model sufficient for the data under consideration, but without giving any detailed comparison. There are many ways to prewhiten data, all of which involve fitting an AR model to the data and transforming the signal to zero-mean white noise with a small variance and a small model estimation error [*Percival and Walden*, 1993]. In general, an nth-order AR model can be used to prewhiten the relative temperature perturbations time series ($x(t)$).

$$w(t) = x(t) - \sum_{n} \varphi_n x(t-n) \tag{5}$$

where φ_n is estimated by solving the Yule-Walker equations and $w(t)$ is very close to white noise with variance σ_w^2 [*Brockwell and Davis*, 2013]. The order (n) of the AR model, which is proportional to the number of spectral peaks in the data, is chosen based on the final prediction error (FPE) criterion.

$$FPE = \sigma_w^2 \left(\frac{N+n}{N-n} \right), \tag{6}$$

where N is the length of the time series [*Brockwell and Davis*, 2013]. We have tested different orders (from first

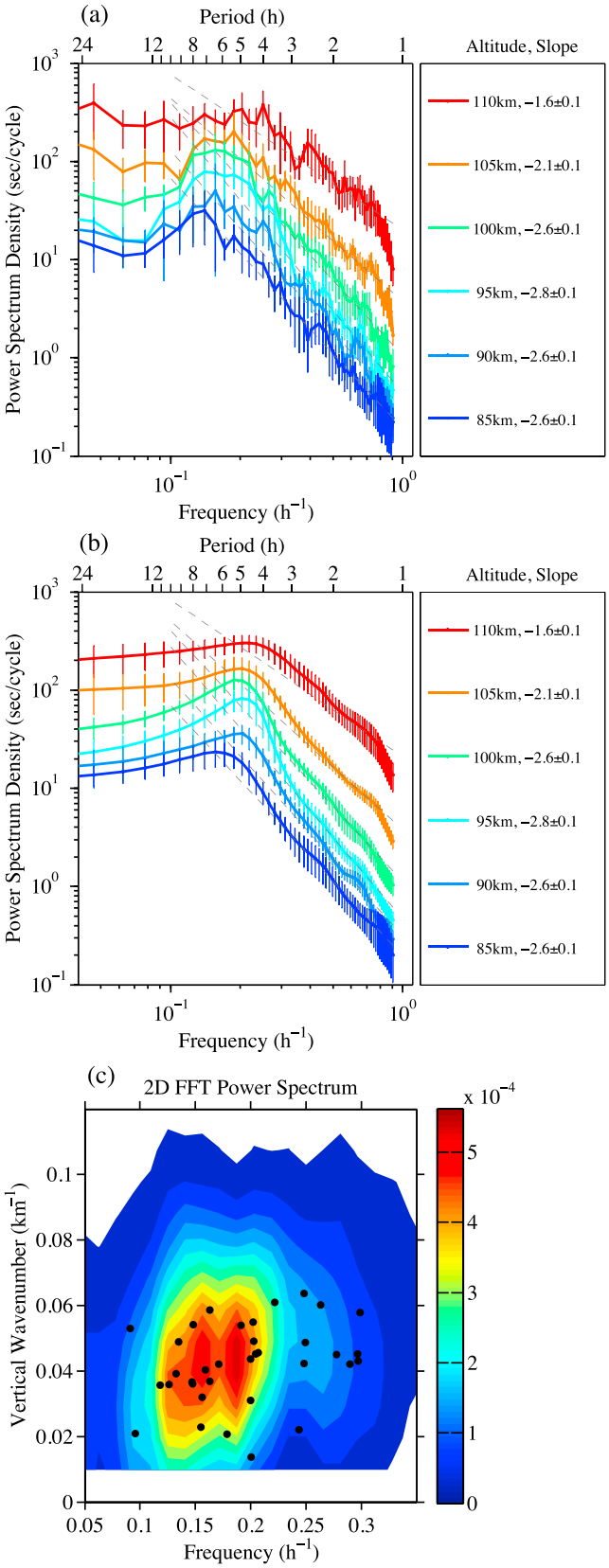

to seventh) of the AR model and found that the FPE decreases significantly from order 1 to order 4 but does not significantly decrease at higher orders. Therefore, we chose the fourth-order AR model to prewhiten our data. The power spectral density ($PSD_w(\omega)$) of the prewhitened data is then calculated using the periodogram method [*Gardner and Voelz*, 1987; *Beatty et al.*, 1992; *Dewan and Grossbard*, 2000].

$$PSD_w(\omega) = \frac{2\delta t}{N}|F_w(\omega)|^2 \qquad (7)$$

where $F_w(\omega)$ is the Fourier transform of $w(t)$. Periodogram of each episode must be calculated at the same frequency grids in order to average results of all episodes. However, each observation length is different in our data sets: the shortest length of all episodes is 12.7 h, while the longest is 64 h. Therefore, we zero-pad the shorter data to 64 h before calculating periodogram. To reduce the variability in the spectral slope estimation, *Dewan and Grossbard* [2000] suggest smoothing the raw $PSD_w(\omega)$. We use a Hamming window with FWHM of 0.25 h^{-1} to smooth $PSD_w(\omega)$. However, such smoothed spectra are not ideal for identifying spectral peaks. Therefore, in order for both peak identification and spectral slope estimation, both raw and smoothed $PSD_w(\omega)$ are postcolored to obtain the PSD of $x(t)$.

$$PSD(\omega) = \frac{PSD_w(\omega)}{\left|1 + \sum_{n=1}^{4} \varphi_n exp(-i\omega n\delta t)\right|^2} \qquad (8)$$

The PSD at each altitude was then vertically averaged every 5 km in order to

Figure 10. (a) Averaged raw frequency PSDs of relative temperature perturbations in June over the 5 years of 2011–2015 at different altitudes. Dotted lines are fittings of the power law shapes in the range of ~1–10 h. The fitted slopes are indicated in the legend. (b) Same as Figure 10a but for smoothed frequency PSDs. (c) Averaged 2-D power spectrum of relative temperature perturbations (dimensionless) in June over the years of 2011–2015. Each black dot line on the contour marks the averaged vertical wavelength and period for each major wave event.

reduce the variance in the spectra and improve accuracy [see *Gardner et al.*, 1989; *Beatty et al.*, 1992]. Finally, the results for each episode in June were weighted by their observation time lengths to obtain weighted-average frequency spectra. The mean raw and smoothed frequency spectra are plotted at increments of 5 km from 85–110 km for June in Figures 10a and 10b, respectively.

Results at different altitudes are denoted by different colors and are indicated in the legends of Figures 10a and 10b. In general, the magnitudes of the power spectra increase with increasing altitudes, with the PSD at 110 km being more than 1 order of magnitude larger than the PSD at 85 km. The absolute magnitudes of the PSDs are comparable to those in the study by *Gardner and Yang* [1998]. We mush be aware that the spectra at periods longer than the total lengths of the original data are less reliable. Because the shortest data set is 12.7 h, spectra longer than 12 h must be interpreted with caution. The raw spectra in Figure 10a show many peaks in the range of 3–10 h, but no consistent peaks at the same periods through 85–110 km. Even though the calculated spectra of the shorter data ($<$64 h) appear to have high-frequency resolution ($\Delta f = 1/64\ \mathrm{h}^{-1}$), the true frequency resolution is lower and is limited by the shorter data length. Therefore, it is not meaningful to discuss these local peaks here. Least squares fittings of the power law spectral shape were done in the period range of 1–10 h, and dashed lines in Figures 10a and 10b denote the fitted spectra. The fitted slopes and their uncertainties at each altitude are also indicated in the legends. The fittings show the same slopes for the raw and smoothed spectra in Figures 10a and 10b, respectively. The slopes are all much steeper at lower altitudes around 85 to 100 km with an average of -2.7. However, from 95 km to 110 km, there is a clear trend in which the slopes gradually become shallower with altitude. At 110 km, the fitted slope becomes -1.6, comparable to the results in previous MLT region GW studies in which the slope was found to be either $-5/3$ or -2 [e.g., *Vincent*, 1984; *Senft and Gardner*, 1991; *Beatty et al.*, 1992; *Nakamura et al.*, 1993; *Senft et al.*, 1993; *Collins et al.*, 1994, 1996; *Gao et al.*, 1998; *Gardner and Yang*, 1998; *Yang et al.*, 2006; *Sivakumar et al.*, 2006]. However, below 110 km, the fitted slopes are significantly steeper than the results shown in previous MLT GW studies, which means that below 110 km, the 3–10 h waves at McMurdo have more excess energy than GWs of the same period band shown in other studies. Another interesting feature is that the transition frequency between the positive and negative slope regions, called the characteristic frequency ω^*, increases with increasing altitude. This trend is more obviously shown in Figure 10b. At 85 km, the corresponding transition period $T^* = 2\pi/\omega^*$ is ~6.7 h, gradually shifting to shorter periods with increasing altitude until T^* is ~4.5 h at 110 km. This shift in T^* could be explained by atmospheric dissipations, since GWs with higher frequencies and, thus, larger vertical phase speeds (presuming vertical wavelengths are the same) are less susceptible to dissipation than those with the same vertical wavelengths, but lower frequencies [*Vadas*, 2005, 2007]. Processes such as wave-induced diffusion, molecular viscosity, and thermal diffusion can all cause dissipation of GWs, and dissipation becomes even stronger when waves propagate above the turbopause (located at ~110 km) [*Weinstock*, 1990; *Vadas*, 2005]. Therefore, the dominant periods of the waves become shorter as altitude increases. Finally, below ω^*, where PSD slopes are usually positive, the spectra gradually flatten as altitude increases. This is especially evident at and above 105 km in Figures 10a and 10b. Spectral leakage from the diurnal and semidiurnal "tides" with fast amplitude growth above 100 km caused by in situ heating/cooling [see *Fong et al.*, 2014, 2015] could have contributed to the flattening.

Vertical spatial spectra of GWs with $\lambda_z < 10$ km in the MLT at McMurdo have been examined by *Lu et al.* [2015b]. They found that the spectra follow the power law for $\lambda_z < 10$ km and that the mean spectral slope ($-p$) is approximately -2.26 in the winter MLT region at McMurdo. Since the 3–10 h waves tend to have longer vertical wavelengths ($\lambda_z \geq 20$ km), in order to study their vertical spatial spectra we focus on a larger vertical wavelength range. Furthermore, inspired by *Collins et al.* [1996], we examine the wave number and frequency dependence of the wave energy simultaneously by calculating the 2-D Fourier transform for each episode in June. The results for each episode are weighted by their observational time lengths and shown in Figure 10c. In order to average the spectra of episodes with different lengths and be consistent with the 1-D frequency spectra shown in Figures 10a and 10b, we use the same zero-padding method in the time domain so that padded data are 64 h long. Furthermore, for sufficient spectral resolution in the long-wavelength part of the spectra, we also zero-pad the data to 1024 points in the vertical domain prior to the transform. Again, we must be aware that the long-wavelength parts ($\lambda_z > 35$ km) of the spectra approach our vertical observation range (80–115 km). As can be seen in Figure 10c, generally, 2-D power spectrum has high powers at λ_z ~20–30 km across periods ~3.5–10 h. Two local peaks appear at $T = 5.3$ h and $T = 6.4$ h; however, since frequency resolution of this averaged spectrum is limited by the shortest data, these peaks should be

interpreted with caution. Each black dot on top of the 2-D power spectrum in Figure 10c is the averaged λ_z and period derived for each major wave event. Most of the derived individual wave parameters coincide well in the higher-power region of the 2-D spectrum. There is a weak positive correlation between period and λ_z; i.e., λ_z tends to increase with increasing period.

5. Discussion

Although several case studies, using simultaneous lidar and MF radar observations, identified some 3–10 h waves as IGWs [*Chen et al.*, 2012, 2013], this is the first report to show that the 3–10 h waves are so persistent that they exist in all lidar observations and that these waves occur year round at McMurdo. The vertical wavelengths of the 3–10 h waves we observed are quite close to that (~25 km) of the "planetary-scale inertio gravity waves" generated by a Numerical Spectral Model [*Mayr*, 2003; *Mayr et al.*, 2004]. These inertio gravity waves appear to have the largest amplitudes from late winter to spring in the polar MLT with periods between 9 and 11 h [*Mayr*, 2003; *Mayr et al.*, 2004]. They are essentially the gravity mode (Class I) solutions to the classical Laplace tidal equations for the Earth's atmosphere, as discussed in the classical literature [*Longuet-Higgins*, 1968]. These simulated features capture some of the observed wave properties but are not consistent with the larger period span (3–10 h) and all-year-round occurrence at McMurdo. Possible identities of the 3–10 h waves, other than gravity waves, include short-period Atmospheric Normal Modes (ANMs), short-period tidal waves, and wave-wave interactions. ANMs, also called Lamb waves, were observed at the South Pole [see *Forbes et al.*, 1999], and can have periods around 3–10 h and a long life span (up to several days) [*Lindzen and Blake*, 1972]. However, theoretically, ANMs have infinite λ_z in an isothermal atmosphere, or a long λ_z (at least ~80 km) in a simulated realistic atmosphere [see *Lindzen and Blake*, 1972; *Forbes et al.*, 1999; *Kovalam and Vincent*, 2003]. As the predicted λ_z of ANMs are much longer than our observed results, the 3–10 h waves are unlikely to be ANMs. As for tidal waves, the vertical wavelengths of subdiurnal tides are generally much larger than those of the 3–10 h waves. Theoretical calculations and model simulations performed by *Smith and Ortland* [2001] indicate that the 8 h tides have a long λ_z (>47 km). Other shorter-period (6 h, 4.8 h, etc.) tidal waves have an even longer λ_z [*Smith*, 2004]. Furthermore, from Figure 9a, there is no phase coherence among different wave events, indicating that the 3–10 h waves are not likely of tidal origin. The observed 3–10 h waves could be the result of wave-wave interactions. For example, based on the measurements from an array of instruments at northern high latitudes, *Wu et al.* [2002] presented revealing observations of a 10 h oscillation in the temperatures and winds in the MLT. By comparing the wave phases at different stations, a zonal wave number $s = 5$ was inferred. These wave properties led to the conclusion that nonlinear coupling between a semidiurnal tide and a 2 day planetary wave was likely the wave origin. However, without observations at different longitudes, we cannot explore the possibilities of such mechanisms.

As the observed 3–10 h waves are unlikely to be ANMs or tides, our current judgment is that they should be regarded as gravity waves, although we cannot rule out the possibility of wave-wave interactions. A challenging question is then—what sources can generate such persistent gravity waves all year round? Although the winter cases may be attributed to unbalanced flow caused by the polar night jet, such a jet is unlikely to exist during the polar summer. *Mayr et al.* [2004] suggest that the planetary-scale inertio gravity waves are excited by instabilities that arise in the zonal mean circulation. Similarly, we may speculate the wave source to be an instability, but there are no clues as to the type of instability. Here we discuss what information on the source can be delineated from the statistical results.

Our frequency spectral analysis of the 3–10 h waves shows differences with the "canonical" wave spectrum, i.e., when waves are regarded as being fully damped or saturated, the PSD follows a form of m^{-p} (m is vertical wave number, $p = 3$ usually) and ω^{-q} [e.g., *VanZandt*, 1982; *Dewan and Good*, 1986; *Smith et al.*, 1987; *Gardner*, 1994]. Many different theories have been proposed to explain the universal wave number spectrum [e.g., *Dewan and Good*, 1986; *Weinstock*, 1990; *Hines*, 1991; *Gardner*, 1994], but fewer theories have been proposed to explain the universal frequency spectrum. Among these are saturated-cascade theory (SCT) [*Dewan*, 1994] and diffusive filtering theory (DFT) [*Gardner*, 1994]. Despite the differences in their mechanisms, SCT and DFT both agree that atmospheric dissipation processes, whether arising from molecular viscosity or eddy diffusion [*Weinstock*, 1990; *Gardner*, 1994], or instability and a turbulent cascade [*Dewan*, 1994], will transfer (diffuse) excess energy from the larger period waves to smaller temporal scale motions (either waves or turbulence). Therefore, it is expected that the slope of the frequency spectrum becomes shallower as it propagates away from the source region

where the slope is steepest [*Gardner*, 1994]. When GWs are saturated, or fully damped, frequency spectra with a ω^{-2} or $\omega^{-5/3}$ trend are predicted from theory [*Dewan*, 1994; *Gardner*, 1994], which is supported by observations in the region where GWs were assumed saturated or fully damped [e.g., *Senft and Gardner*, 1991; *Beatty et al.*, 1992; *Senft et al.*, 1993; *Gardner and Yang*, 1998]. On the other hand, a steeper slope implies that the observed wave spectrum still bears some resemblance to the source spectrum, which means that the dissipation effects have not yet changed the shape of the spectrum to a fully damped or saturated shape. This is likely the case for our data below 105 km. As the wavefield propagates upward, atmospheric dissipation processes remove low-frequency energy, and therefore, the observed spectrum becomes increasingly shallower than the source. This prediction matches our observation that the slopes gradually become shallower with increasing altitude. The phenomena observed at McMurdo imply that the wave source(s) of these 3–10 h wave may not be far from the MLT region, unlike at middle-low latitudes where major sources of the MLT gravity waves, such as convection, topography, or tropospheric jet streams, are located in the troposphere [see *Fritts and Alexander*, 2003; *Alexander et al.*, 2010]. Our results likely point to a wave source in the stratosphere, which is consistent with the speculation of the wave source for the 7.7 h wave (unbalanced flow in the polar vortex ~40 km) by *Chen et al.* [2013] in a case study. In fact, it is known that stratospheric sources are important for Antarctic gravity waves, as supported by many gravity wave studies [e.g., *Yoshiki and Sato*, 2000; *Sato and Yoshiki*, 2008; *Yamashita et al.*, 2009; *Yamashita*, 2011; *Moffat-Griffin et al.*, 2013; *Murphy et al.*, 2014].

The universal peaks at λ_z ~20–30 km across periods ~3.5–10 h shown in the 2D-FFT results are "characteristic vertical wavelengths" that mark the transition between the source and the so-called "saturated" regimes of the spectrum [*Smith et al.*, 1987]. These uniform, dominant vertical wavelengths could provide a hint as to the vertical scale of the sources because the strongest GW response tends to occur at a vertical wavelength about twice the depth of the forcing region [*Vadas and Fritts*, 2001; *Fritts and Alexander*, 2003; *Alexander and Holton*, 2004]. Using a similar heuristic argument as *Fritts and Alexander* [2003], we can estimate the approximate vertical scale of the wave sources. Since the vertical wavelength is inversely proportional to the buoyancy frequency N (equation (33) in *Fritts and Alexander*, 2003), and N in the Antarctic winter mesosphere is about 2/3 of its value in the stratosphere [*Lu et al.*, 2015b], the λ_z of the 3–10 h wave in the stratosphere should, by the above argument, be ~2/3 of its MLT value, or ~16 km. Therefore, if it were a stratospheric source, the vertical scale of the forcing region might be ~8 km. This information might be useful in future studies on the wave source location, although we are aware that it is only a speculation for now.

6. Conclusions and Outlooks

To our knowledge, this study is the first to report the persistence of the 3–10 h gravity waves in the polar MLT region. During the last 5 years of lidar observations at McMurdo, the group of 3–10 h waves has been perpetual. That is, such waves occur on every lidar run spanning a sufficient duration, and so far we have not seen any inactive wave gap epoch in the lidar temperature data. In order to accurately quantify the lifetime and occurrence of these 3–10 h waves, we have demonstrated a new wave analysis method in a case study using ~65 h of lidar data from 28 to 30 June 2014 at McMurdo. A rectified wavelet function is used in a wavelet transform of relative temperature perturbations to give an accurate, unbiased estimate of the wave amplitudes for all periods in a 1-D time series. Dominant wave packets are identified through searching the amplitude contours on the wavelet power spectrum for each altitude. Vertical coherence of waves at multiple altitudes is then examined to determine the major wave events. Following this, the major wave perturbations are extracted using wavelet reconstruction. This improved wavelet function, in combination with the temporal wavelet reconstruction and some spatial scrutiny, enables us to quantify the life span, occurrence rate, and many other properties of the waves in a systematic manner. Applying this new analysis method to all of the lidar data recorded during the month of June in the years of 2011–2015, the statistical results of wave properties, such as occurrence frequencies, periods, phases, vertical wavelengths, and vertical phase speeds, are obtained for McMurdo (77.8°S, 166.7°E), Antarctica. In general, these waves have periods of 3–10 h, vertical wavelengths of 20–30 km, and vertical phase speeds of ~0.8–2 m/s. These waves have dominant amplitudes in the MLT and extremely long lifetimes (sometimes ~60 h observed). The occurrence frequencies of these 3–10 h waves are high. Waves with periods of ~3.5, 5, 6–6.5, and 7.5 h have the highest occurrence frequencies each occurring more than 25% of the time in 323 h of data examined. Furthermore, on average, 93% of time, the 3–10 h waves possess more than half of the spectral energy. The relatively slow vertical phase speeds and short vertical wavelengths make these 3–10 h waves very susceptible to damping in thermosphere diffusions. Therefore, the momentum flux, heat flux, and atmospheric constituent flux

associated with these waves have the potential to alter the mean flow, temperature structure, and constituent concentrations in the Antarctic lower thermosphere.

The frequency spectra of these 3–10 h waves have also been examined using a rigorous method of "prewhitening and postcoloring." To our knowledge, this study is the first to show how GW temperature frequency spectra evolve with altitude in the MLT region. By fitting the spectra with a power law spectral shape in the period range of 1–10 h, we find an interesting phenomenon for the 3–10 h waves at McMurdo. That is, the spectral slopes are unusually steep, with an averaged value of −2.7, below 100 km, gradually becoming shallower to −1.6 at 110 km. From this, we speculate that the source region is close to the MLT region, which points to a possible stratospheric source. The characteristic periods in the spectra show a clear trend toward shorter periods with increasing altitude. Such a variation is expected, considering that the effect of atmospheric dissipations is to remove waves with longer periods, especially around the turbopause region. From the 2-D FFT spectra, these waves have peak powers at vertical wavelengths of ~20–30 km across periods of ~3.5–10 h. This uniform peak λ_z across the different periods might shed some light on the vertical scale of the wave sources. Many features of the 3–10 h waves challenge our understanding of gravity waves and demand deeper investigation into the sources and mechanisms for their generation, the reasons for their persistence, and their impacts on general circulation and chemical climate models. We cannot answer these important questions without further studying our Rayleigh lidar data and investigating the high-resolution global models and assimilated data sets.

Acknowledgments

We sincerely acknowledge invaluable discussions with Chester S. Gardner, Rich Collins, and Takuji Nakamura on the lidar data analysis, and with Elsayed Talaat and Jeff Forbes on the wave identity. We are grateful to Wentao Huang, Zhangjun Wang, and Ian Barry for their contributions, and to Vladimir Papitashvili, Julie Palais, Richard Dean, and Judy Shiple for their guidance and support of the McMurdo lidar campaign. We appreciate the staff of the United States Antarctic Program, McMurdo station, Antarctica New Zealand, and Scott Base for their superb support. This work was supported by National Science Foundation (NSF) grants ANT-0839091 and PLR-1246405. Cao Chen was partially supported by AGS-1136272 and CIRES Graduate Student Research Award. Xian Lu was partially supported by NSF/CEDAR grant AGS-1343106. John A. Smith was partially supported by NSF grants AGS-1452351 and AGS-1115224. Data necessary to reproduce the results are available from the authors upon request (xinzhao.chu@colorado.edu).

References

Alexander, M. J., and J. R. Holton (2004), On the spectrum of vertically propagating gravity waves generated by a transient heat source, *Atmos. Chem. Phys.*, *4*(4), 923–932, doi:10.5194/acp-4-923-2004.

Alexander, M. J., and L. Pfister (1995), Gravity wave momentum flux in the lower stratosphere over convection, *Geophys. Res. Lett.*, *22*(15), 2029–2032, doi:10.1029/95GL01984.

Alexander, M. J., et al. (2008), Global estimates of gravity wave momentum flux from High Resolution Dynamics Limb Sounder observations, *J. Geophys. Res.*, *113*, D15S18, doi:10.1029/2007JD008807.

Alexander, M. J., et al. (2010), Recent developments in gravity-wave effects in climate models and the global distribution of gravity-wave momentum flux from observations and models, *Q. J. R. Meteorol. Soc.*, *136*, 1103–1124, doi:10.1002/qj.637.

Allen, S. J., and R. A. Vincent (1995), Gravity wave activity in the lower atmosphere: Seasonal and latitudinal variations, *J. Geophys. Res.*, *100*(D1), 1327, doi:10.1029/94JD02688.

Azeem, S. M. I., and G. G. Sivjee (2009), Multiyear observations of tidal oscillations in OH M(3,1) rotational temperatures at South Pole, Antarctica, *J. Geophys. Res.*, *114*, A06312, doi:10.1029/2008JA013976.

Baumgaertner, A. J. G., A. J. McDonald, G. J. Fraser, and G. E. Plank (2005), Long-term observations of mean winds and tides in the upper mesosphere and lower thermosphere above Scott Base, Antarctica, *J. Atmos. Sol. Terr. Phys.*, *67*(16), 1480–1496, doi:10.1016/j.jastp.2005.07.018.

Beatty, T. J., C. A. Hostetler, and C. S. Gardner (1992), Lidar observations of gravity waves and their spectra near the mesopause and stratopause at Arecibo, *J. Atmos. Sci.*, *49*(6), 477–496, doi:10.1175/1520-0469(1992)049<0477:LOOGWA>2.0.CO;2.

Brockwell, P. J., and R. A. Davis (2013), *Time Series: Theory and Methods*, Springer, New York.

Chen, C., X. Chu, Z. Yu, W. Fong, A. J. McDonald, X. Lu, and W. Huang (2012), Lidar and radar investigation of inertia gravity wave intrinsic properties at McMurdo, Antarctica, in *Proceedings of the 26th International Laser Radar Conference*, pp. 1057–1060, Porto Heli, Greece.

Chen, C., X. Chu, A. J. McDonald, S. L. Vadas, Z. Yu, W. Fong, and X. Lu (2013), Inertia-gravity waves in Antarctica: A case study using simultaneous lidar and radar measurements at McMurdo/Scott Base (77.8°S, 166.7°E), *J. Geophys. Res. Atmos.*, *118*, 2794–2808, doi:10.1002/jgrd.50318.

Chu, X., W. Pan, G. C. Papen, C. S. Gardner, and J. A. Gelbwachs (2002), Fe boltzmann temperature lidar: Design, error analysis, and initial results at the North and South Poles, *Appl. Opt.*, *41*(21), 4400, doi:10.1364/AO.41.004400.

Chu, X., C. S. Gardner, and S. J. Franke (2005), Nocturnal thermal structure of the mesosphere and lower thermosphere region at Maui, Hawaii (20.7°N), and Starfire Optical Range, New Mexico (35°N), *J. Geophys. Res.*, *110*, D09S03, doi:10.1029/2004JD004891.

Chu, X., W. Huang, W. Fong, Z. Yu, Z. Wang, J. A. Smith, and C. S. Gardner (2011a), First lidar observations of polar mesospheric clouds and Fe temperatures at McMurdo (77.8°S, 166.7°E), Antarctica, *Geophys. Res. Lett.*, *38*, L16810, doi:10.1029/2011GL048373.

Chu, X., Z. Yu, C. S. Gardner, C. Chen, and W. Fong (2011b), Lidar observations of neutral Fe layers and fast gravity waves in the thermosphere (110–155 km) at McMurdo (77.8°S, 166.7°E), Antarctica, *Geophys. Res. Lett.*, *38*, L23807, doi:10.1029/2011GL050016.

Collins, R., and C. Gardner (1995), Gravity wave activity in the stratosphere and mesosphere at the South Pole, *Adv. Space Res.*, *16*(5), 81–90, doi:10.1016/0273-1177(95)00175-E.

Collins, R. L., A. Nomura, and C. S. Gardner (1994), Gravity waves in the upper mesosphere over Antarctica: Lidar observations at the South Pole and Syowa, *J. Geophys. Res.*, *99*(D3), 5475, doi:10.1029/93JD03276.

Collins, R. L., X. Tao, and C. S. Gardner (1996), Gravity wave activity in the upper mesosphere over Urbana, Illinois: Lidar observations and analysis of gravity wave propagation models, *J. Atmos. Terr. Phys.*, *58*(16), 1905–1926, doi:10.1016/0021-9169(96)00026-8.

Dewan, E. M. (1994), The saturated-cascade model for atmospheric gravity wave spectra, and the wavelength-period (W-P) relations, *Geophys. Res. Lett.*, *21*(9), 817–820, doi:10.1029/94GL00702.

Dewan, E. M., and N. Grossbard (2000), Power spectral artifacts in published balloon data and implications regarding saturated gravity wave theories, *J. Geophys. Res.*, *105*(D4), 4667, doi:10.1029/1999JD901108.

Dewan, E. M., and R. E. Good (1986), Saturation and the "universal" spectrum for vertical profiles of horizontal scalar winds in the atmosphere, *J. Geophys. Res.*, *91*(D2), 2742, doi:10.1029/JD091iD02p02742.

Diettrich, J. C., G. J. Nott, P. J. Espy, X. Chu, and D. Riggin (2006), Statistics of sporadic iron layers and relation to atmospheric dynamics, *J. Atmos. Sol. Terr. Phys.*, *68*(1), 102–113, doi:10.1016/j.jastp.2005.08.008.

Dowdy, A. J. (2004), The large-scale dynamics of the mesosphere–lower thermosphere during the Southern Hemisphere stratospheric warming of 2002, *Geophys. Res. Lett.*, *31*, L14102, doi:10.1029/2004GL020282.

Eckermann, S. D., and P. Preusse (1999), Global measurements of stratospheric mountain waves from space, *Science*, *286*(5444), 1534–1537, doi:10.1126/science.286.5444.1534.

Espy, P. J., R. E. Hibbins, D. M. Riggin, and D. C. Fritts (2005), Mesospheric planetary waves over Antarctica during 2002, *Geophys. Res. Lett.*, *32*, L21804, doi:10.1029/2005GL023886.

Espy, P. J., R. E. Hibbins, G. R. Swenson, J. Tang, M. J. Taylor, D. M. Riggin, and D. C. Fritts (2006), Regional variations of mesospheric gravity-wave momentum flux over Antarctica, *Ann. Geophys.*, *24*(1), 81–88, doi:10.5194/angeo-24-81-2006.

Eyring, V., et al. (2006), Assessment of temperature, trace species, and ozone in chemistry-climate model simulations of the recent past, *J. Geophys. Res.*, *111*, D22308, doi:10.1029/2006JD007327.

Fong, W., X. Lu, X. Chu, T. J. Fuller-Rowell, Z. Yu, B. R. Roberts, C. Chen, C. S. Gardner, and A. J. McDonald (2014), Winter temperature tides from 30 to 110 km at McMurdo (77.8°S, 166.7°E), Antarctica: Lidar observations and comparisons with WAM, *J. Geophys. Res. Atmos.*, *119*, 2846–2863, doi:10.1002/2013JD020784.

Fong, W., X. Chu, X. Lu, C. Chen, T. J. Fuller-Rowell, M. Codrescu, and A. D. Richmond (2015), Lidar and CTIPe model studies of the fast amplitude growth with altitude of the diurnal temperature "tides" in the Antarctic winter lower thermosphere and dependence on geomagnetic activity, *Geophys. Res. Lett.*, *42*, 697–704, doi:10.1002/2014GL062784.

Forbes, J. M., N. A. Makarov, and Y. I. Portnyagin (1995), First results from the meteor radar at South Pole: A large 12-hour oscillation with zonal wavenumber one, *Geophys. Res. Lett.*, *22*(23), 3247–3250, doi:10.1029/95GL03370.

Forbes, J. M., S. E. Palo, X. Zhang, Y. I. Portnyagin, N. A. Makarov, and E. G. Merzlyakov (1999), Lamb waves in the lower thermosphere: Observational evidence and global consequences, *J. Geophys. Res.*, *104*(A8), 17107, doi:10.1029/1999JA900044.

Friedman, J. S., and X. Chu (2007), Nocturnal temperature structure in the mesopause region over the Arecibo Observatory (18.35°N, 66.75°W): Seasonal variations, *J. Geophys. Res.*, *112*, D14107, doi:10.1029/2006JD008220.

Fritts, D. C. (1984), Gravity wave saturation in the middle atmosphere: A review of theory and observations, *Rev. Geophys.*, *22*(3), 275–308, doi:10.1029/RG022i003p00275.

Fritts, D. C., and M. J. Alexander (2003), Gravity wave dynamics and effects in the middle atmosphere, *Rev. Geophys.*, *41*(1), 1003, doi:10.1029/2001RG000106.

Gao, X., J. W. Meriwether, V. B. Wickwar, T. D. Wilkerson, and S. Collins (1998), Rayleigh lidar measurements of the temporal frequency and vertical wavenumber spectra in the mesosphere over the Rocky Mountain region, *J. Geophys. Res.*, *103*(D6), 6405–6416, doi:10.1029/97JD03073.

Garcia, R. R., and B. A. Boville (1994), "Downward control" of the mean meridional circulation and temperature distribution of the polar winter stratosphere, *J. Atmos. Sci.*, *51*(15), 2238–2245, doi:10.1175/1520-0469(1994)051<2238:COTMMC>2.0.CO;2.

Gardner, C. S. (1994), Diffusive filtering theory of gravity wave spectra in the atmosphere, *J. Geophys. Res.*, *99*(D10), 20,601–20,622, doi:10.1029/94JD00819.

Gardner, C. S., and D. G. Voelz (1987), Lidar studies of the nighttime sodium layer over Urbana, Illinois: 2. Gravity waves, *J. Geophys. Res.*, *92*(A5), 4673–4694, doi:10.1029/JA092iA05p04673.

Gardner, C. S., and W. Yang (1998), Measurements of the dynamical cooling rate associated with the vertical transport of heat by dissipating gravity waves in the mesopause region at the Starfire Optical Range, New Mexico, *J. Geophys. Res.*, *103*(D14), 16,909–16,926, doi:10.1029/98JD00683.

Gardner, C. S., D. C. Senft, T. J. Beatty, R. E. Bills, and C. A. Hosteler (1989), Rayleigh and sodium lidar techniques for measuring middle atmospheric density, temperature and wind perturbation and their spectra, in *World Ionsphere/Thermosphere Study Handbook*, vol. 2, edited by C. H. Liu and B. Edwards, pp. 148–187, International Congress of Scientific Unions, Urbana.

Gelbwachs, J. A. (1994), Iron Boltzmann factor LIDAR: Proposed new remote-sensing technique for mesospheric temperature, *Appl. Opt.*, *33*(30), 7151–7156.

Hauchecorne, A., and M.-L. Chanin (1980), Density and temperature profiles obtained by lidar between 35 and 70 km, *Geophys. Res. Lett.*, *7*(8), 565–568, doi:10.1029/GL007i008p00565.

Hernandez, G., R. W. Smith, G. J. Fraser, and W. L. Jones (1992), Large-scale waves in the upper-mesosphere at Antarctic high-latitudes, *Geophys. Res. Lett.*, *19*(13), 1347–1350, doi:10.1029/92GL01281.

Hertzog, A., M. J. Alexander, and R. Plougonven (2012), On the intermittency of gravity wave momentum flux in the stratosphere, *J. Atmos. Sci.*, *69*(11), 3433–3448, doi:10.1175/JAS-D-12-09.1.

Hibbins, R. E., P. J. Espy, M. J. Jarvis, D. M. Riggin, and D. C. Fritts (2007), A climatology of tides and gravity wave variance in the MLT above Rothera, Antarctica obtained by MF radar, *J. Atmos. Sol. Terr. Phys.*, *69*(4–5), 578–588, doi:10.1016/j.jastp.2006.10.009.

Hines, C. O. (1991), The saturation of gravity waves in the middle atmosphere. Part II: Development of doppler-spread theory, *J. Atmos. Sci.*, *48*(11), 1361–1379, doi:10.1175/1520-0469(1991)048<1361:TSOGWI>2.0.CO;2.

Hocke, K., and N. Kämpfer (2009), Gap filling and noise reduction of unevenly sampled data by means of the Lomb-Scargle periodogram, *Atmos. Chem. Phys.*, *9*(12), 4197–4206, doi:10.5194/acp-9-4197-2009.

Iimura, H., S. E. Palo, Q. Wu, T. L. Killeen, S. C. Solomon, and W. R. Skinner (2009), Structure of the nonmigrating semidiurnal tide above Antarctica observed from the TIMED Doppler Interferometer, *J. Geophys. Res.*, *114*, D11102, doi:10.1029/2008JD010608.

Kovalam, S., and R. A. Vincent (2003), Intradiurnal wind variations in the midlatitude and high-latitude mesosphere and lower thermosphere, *J. Geophys. Res.*, *108*(D4), 4135, doi:10.1029/2002JD002500.

Lindzen, R. S., and D. Blake (1972), Lamb waves in the presence of realistic distributions of temperature and dissipation, *J. Geophys. Res.*, *77*(12), 2166–2176, doi:10.1029/JC077i012p02166.

Liu, Y., X. San Liang, and R. H. Weisberg (2007), Rectification of the bias in the wavelet power spectrum, *J. Atmos. Oceanic Technol.*, *24*(12), 2093–2102, doi:10.1175/2007JTECHO511.1.

Longuet-Higgins, M. S. (1968), The eigenfunctions of Laplace's tidal equations over a sphere, *Philos. Trans. R. Soc., A*, *262*(1132), 511–607, doi:10.1098/rsta.1968.0003.

Lu, X., X. Chu, T. Fuller-Rowell, L. Chang, W. Fong, and Z. Yu (2013), Eastward propagating planetary waves with periods of 1–5 days in the winter Antarctic stratosphere as revealed by MERRA and lidar, *J. Geophys. Res. Atmos.*, *118*, 9565–9578, doi:10.1002/jgrd.50717.

Lu, X., C. Chen, W. Huang, J. A. Smith, X. Chu, T. Yuan, P.-D. Pautet, M. J. Taylor, J. Gong, and C. Y. Cullens (2015a), A coordinated study of 1 h mesoscale gravity waves propagating from Logan to Boulder with CRRL Na Doppler lidars and temperature mapper, *J. Geophys. Res. Atmos.*, *120*, 10,006–10,021, doi:10.1002/2015JD023604.

Lu, X., X. Chu, W. Fong, C. Chen, Z. Yu, B. R. Roberts, and A. J. McDonald (2015b), Vertical evolution of potential energy density and vertical wavenumber spectrum of Antarctic gravity waves from 35 to 105 km at McMurdo (77.8°S, 166.7°E), *J. Geophys. Res. Atmos.*, *120*, 2719–2737, doi:10.1002/2014JD022751.

Mayr, H. G. (2003), Planetary-scale inertio gravity waves in the Mesosphere, *Geophys. Res. Lett.*, *30*(23), 2228, doi:10.1029/2003GL018376.

Mayr, H. G., J. G. Mengel, E. R. Talaat, H. S. Porter, and K. L. Chan (2004), Properties of internal planetary-scale inertio gravity waves in the mesosphere, *Ann. Geophys.*, *22*(10), 3421–3435, doi:10.5194/angeo-22-3421-2004.
McDonald, A. J., B. Tan, and X. Chu (2010), Role of gravity waves in the spatial and temporal variability of stratospheric temperature measured by COSMIC/FORMOSAT-3 and Rayleigh lidar observations, *J. Geophys. Res.*, *115*, D19128, doi:10.1029/2009JD013658.
McLandress, C., T. G. Shepherd, S. Polavarapu, and S. R. Beagley (2012), Is missing orographic gravity wave drag near 60°S the cause of the stratospheric zonal wind biases in chemistry–climate models?, *J. Atmos. Sci.*, *69*(3), 802–818, doi:10.1175/JAS-D-11-0159.1.
Moffat-Griffin, T., M. J. Jarvis, S. R. Colwell, A. J. Kavanagh, G. L. Manney, and W. H. Daffer (2013), Seasonal variations in lower stratospheric gravity wave energy above the Falkland Islands, *J. Geophys. Res. Atmos.*, *118*, 10,861–10,869, doi:10.1002/jgrd.50859.
Morris, R. J., A. R. Klekociuk, and D. A. Holdsworth (2009), Low latitude 2-day planetary wave impact on austral polar mesopause temperatures: Revealed by a January diminution in PMSE above Davis, Antarctica, *Geophys. Res. Lett.*, *36*, L11807, doi:10.1029/2009GL037817.
Murphy, D. J., et al. (2006), A climatology of tides in the Antarctic mesosphere and lower thermosphere, *J. Geophys. Res.*, *111*, D23104, doi:10.1029/2005JD006803.
Murphy, D. J., S. P. Alexander, A. R. Klekociuk, P. T. Love, and R. A. Vincent (2014), Radiosonde observations of gravity waves in the lower stratosphere over Davis, Antarctica, *J. Geophys. Res. Atmos.*, *119*, 11,973–11,996, doi:10.1002/2014JD022448.
Nakamura, T., T. Tsuda, M. Yamamoto, S. Fukao, and S. Kato (1993), Characteristics of gravity waves in the mesosphere observed with the middle and upper atmosphere radar: 2. Propagation direction, *J. Geophys. Res.*, *98*(D5), 8911–8923, doi:10.1029/92JD03030.
Nappo, C. J. (2002), *An Introduction to Atmospheric Gravity Waves*, Academic Press, San Diego, Calif.
Nielsen, K., M. J. Taylor, R. E. Hibbins, M. J. Jarvis, and J. M. Russell (2012), On the nature of short-period mesospheric gravity wave propagation over Halley, Antarctica, *J. Geophys. Res.*, *117*, D05124, doi:10.1029/2011JD016261.
Nomura, A., T. Kano, Y. Iwasaka, H. Fukunishi, T. Hirasawa, and S. Kawaguchi (1987), Lidar observations of the mesospheric sodium layer at Syowa Station, Antarctica, *Geophys. Res. Lett.*, *14*(7), 700–703, doi:10.1029/GL014i007p00700.
Percival, D. B., and A. T. Walden (1993), *Spectral Analysis for Physical Applications*, Cambridge Univ. Press, Cambridge.
Pfister, L., K. R. Chan, T. P. Bui, S. Bowen, M. Legg, B. Gary, K. Kelly, M. Proffitt, and W. Starr (1993), Gravity waves generated by a tropical cyclone during the STEP tropical field program: A case study, *J. Geophys. Res.*, *98*(D5), 8611–8638, doi:10.1029/92JD01679.
Plougonven, R., A. Hertzog, and H. Teitelbaum (2008), Observations and simulations of a large-amplitude mountain wave breaking over the Antarctic Peninsula, *J. Geophys. Res.*, *113*, D16113, doi:10.1029/2007JD009739.
Portnyagin, Y. I., J. M. Forbes, E. G. Merzlyakov, N. A. Makarov, and S. E. Palo (2000), Intradiurnal wind variations observed in the lower thermosphere over the South Pole, *Ann. Geophys.*, *18*(5), 547–554, doi:10.1007/s00585-000-0547-3.
Sato, K., and M. Yamada (1994), Vertical structure of atmospheric gravity waves revealed by the wavelet analysis, *J. Geophys. Res.*, *99*(D10), 20,623–20,631, doi:10.1029/94JD01818.
Sato, K., and M. Yoshiki (2008), Gravity wave generation around the polar vortex in the stratosphere revealed by 3-hourly radiosonde observations at syowa station, *J. Atmos. Sci.*, *65*(12), 3719–3735, doi:10.1175/2008jas2539.1.
Scargle, J. D. (1989), Studies in astronomical time series analysis. III - Fourier transforms, autocorrelation functions, and cross-correlation functions of unevenly spaced data, *Astrophys. J.*, *343*, 874–887, doi:10.1086/167757.
Senft, D. C., and C. S. Gardner (1991), Seasonal variability of gravity wave activity and spectra in the mesopause region at Urbana, *J. Geophys. Res.*, *96*(D9), 17,229–17,264, doi:10.1029/91JD01662.
Senft, D., C. Hostetler, and C. Gardner (1993), Characteristics of gravity wave activity and spectra in the upper stratosphere and upper mesosphere at Arecibo during early April 1989, *J. Atmos. Terr. Phys.*, *55*(3), 425–439, doi:10.1016/0021-9169(93)90078-D.
She, C. Y., et al. (2004), Tidal perturbations and variability in the mesopause region over Fort Collins, CO (41°N, 105°W): Continuous multi-day temperature and wind lidar observations, *Geophys. Res. Lett.*, *31*, L24111, doi:10.1029/2004GL021165.
Sivakumar, V., P. B. Rao, and H. Bencherif (2006), Lidar observations of middle atmospheric gravity wave activity over a low-latitude site (Gadanki, 13.5°N, 79.2°E), *Ann. Geophys.*, *24*(3), 823–834, doi:10.5194/angeo-24-823-2006.
Sivjee, G. G., and R. L. Walterscheid (1994), Six-hour zonally symmetric tidal oscillations of the winter mesopause over the South Pole Station, *Planet. Space Sci.*, *42*(6), 447–453, doi:10.1016/0032-0633(94)00085-9.
Smith, A. K. (2004), Observations and modeling of the 6-hour tide in the upper mesosphere, *J. Geophys. Res.*, *109*, D10105, doi:10.1029/2003JD004421.
Smith, A. K., and D. A. Ortland (2001), Modeling and analysis of the structure and generation of the terdiurnal tide, *J. Atmos. Sci.*, *58*(21), 3116–3134, doi:10.1175/1520-0469(2001)058<3116:MAAOTS>2.0.CO;2.
Smith, S. A., D. C. Fritts, and T. E. Vanzandt (1987), Evidence for a saturated spectrum of atmospheric gravity waves, *J. Atmos. Sci.*, *44*(10), 1404–1410, doi:10.1175/1520-0469(1987)044<1404:EFASSO>2.0.CO;2.
States, R. J., and C. S. Gardner (2000), Thermal structure of the mesopause region (80–105 km) at 40°N latitude. Part II: Diurnal variations, *J. Atmos. Sci.*, *57*(1), 78–92, doi:10.1175/1520-0469(2000)057<0078:TSOTMR>2.0.CO;2.
Suzuki, S., M. Tsutsumi, S. E. Palo, Y. Ebihara, M. Taguchi, and M. Ejiri (2011), Short-period gravity waves and ripples in the South Pole mesosphere, *J. Geophys. Res.*, *116*, D19109, doi:10.1029/2011JD015882.
Tan, B., H.-L. Liu, and X. Chu (2011), Studying the "cold pole" problem in WACCM and comparison to lidar temperature morphology, presented at the AGU Fall Meeting 2011 (SA31B-1973), San Francisco, Calif, December 7.
Torrence, C., and G. P. Compo (1998), A Practical Guide to Wavelet Analysis, *Bull. Am. Meteorol. Soc.*, *79*(1), 61–78, doi:10.1175/1520-0477(1998)079<0061:APGTWA>2.0.CO;2.
Tsuda, T., S. Kato, T. Yokoi, T. Inoue, M. Yamamoto, T. E. VanZandt, S. Fukao, and T. Sato (1990), Gravity waves in the mesosphere observed with the middle and upper atmosphere radar, *Radio Sci.*, *25*(5), 1005–1018, doi:10.1029/RS025i005p01005.
Vadas, S. L. (2005), Thermospheric responses to gravity waves: Influences of increasing viscosity and thermal diffusivity, *J. Geophys. Res.*, *110*, D15103, doi:10.1029/2004JD005574.
Vadas, S. L. (2007), Horizontal and vertical propagation and dissipation of gravity waves in the thermosphere from lower atmospheric and thermospheric sources, *J. Geophys. Res.*, *112*, A06305, doi:10.1029/2006JA011845.
Vadas, S. L., and D. C. Fritts (2001), Gravity wave radiation and mean responses to local body forces in the atmosphere, *J. Atmos. Sci.*, *58*(16), 2249–2279, doi:10.1175/1520-0469(2001)058<2249:GWRAMR>2.0.CO;2.
Vadas, S. L., and D. C. Fritts (2006), Influence of solar variability on gravity wave structure and dissipation in the thermosphere from tropospheric convection, *J. Geophys. Res.*, *111*, A10S12, doi:10.1029/2005JA011510.
VanZandt, T. E. (1982), A universal spectrum of buoyancy waves in the atmosphere, *Geophys. Res. Lett.*, *9*(5), 575–578, doi:10.1029/GL009i005p00575.
Vincent, R. A. (1984), Gravity-wave motions in the mesosphere, *J. Atmos. Terr. Phys.*, *46*(2), 119–128, doi:10.1016/0021-9169(84)90137-5.
Vincent, R. A. (1994), Gravity-wave motions in the mesosphere and lower thermosphere observed at Mawson, Antarctica, *J. Atmos. Terr. Phys.*, *56*(5), 593–602, doi:10.1016/0021-9169(94)90100-7.

Wang, L., D. C. Fritts, B. P. Williams, R. A. Goldberg, F. J. Schmidlin, and U. Blum (2006), Gravity waves in the middle atmosphere during the MaCWAVE winter campaign: Evidence of mountain wave critical level encounters, *Ann. Geophys.*, *24*(4), 1209–1226, doi:10.5194/angeo-24-1209-2006.

Wang, Z., X. Chu, W. Huang, W. Fong, J. A. Smith, and B. Roberts (2012), Refurbishment and upgrade of Fe Boltzmann/Rayleigh temperature lidar at Boulder for McMurdo lidar campaign in Antarctica, in *Proceeding of the 26th International Laser Radar Conference*, pp. 207–210, Porto Heli, Greece.

Weinstock, J. (1990), Saturated and unsaturated spectra of gravity waves and scale-dependent diffusion, *J. Atmos. Sci.*, *47*(18), 2211–2226, doi:10.1175/1520-0469(1990)047<2211:SAUSOG>2.0.CO;2.

Werner, R., K. Stebel, G. H. Hansen, U. Blum, U.-P. Hoppe, M. Gausa, and K.-H. Fricke (2007), Application of wavelet transformation to determine wavelengths and phase velocities of gravity waves observed by lidar measurements, *J. Atmos. Sol. Terr. Phys.*, *69*(17–18), 2249–2256, doi:10.1016/j.jastp.2007.05.013.

Wu, Q., T. L. Killeen, D. McEwen, S. C. Solomon, W. Guo, G. G. Sivjee, and J. M. Reeves (2002), Observation of the mesospheric and lower thermospheric 10-hour wave in the northern polar region, *J. Geophys. Res.*, *107*(A6), 1082, doi:10.1029/2001JA000192.

Wu, Q., N. J. Mitchell, T. L. Killeen, S. C. Solomon, and P. T. Younger (2005), A high-latitude 8-hour wave in the mesosphere and lower thermosphere, *J. Geophys. Res.*, *110*, A09301, doi:10.1029/2005JA011024.

Yamashita, C. (2011), *Atmospheric Coupling Through Gravity Waves During Stratospheric Sudden Warmings: Gravity Wave Variations, Generation Mechanisms, and Impacts*, Univ. of Colo., Boulder, Colo.

Yamashita, C., X. Chu, H.-L. Liu, P. J. Espy, G. J. Nott, and W. Huang (2009), Stratospheric gravity wave characteristics and seasonal variations observed by lidar at the South Pole and Rothera, Antarctica, *J. Geophys. Res.*, *114*, D12101, doi:10.1029/2008JD011472.

Yang, G., B. Clemesha, P. Batista, and D. Simonich (2006), Gravity wave parameters and their seasonal variations derived from Na lidar observations at 23°S, *J. Geophys. Res.*, *111*, D21107, doi:10.1029/2005JD006900.

Yang, G., B. Clemesha, P. Batista, and D. Simonich (2010), Seasonal variations of gravity wave activity and spectra derived from sodium temperature lidar, *J. Geophys. Res.*, *115*, D18104, doi:10.1029/2009JD012367.

Yoshiki, M., and K. Sato (2000), A statistical study of gravity waves in the polar regions based on operational radiosonde data, *J. Geophys. Res.*, *105*(D14), 17,995–18,011, doi:10.1029/2000JD900204.

Yu, Z., X. Chu, W. Huang, W. Fong, and B. R. Roberts (2012), Diurnal variations of the Fe layer in the mesosphere and lower thermosphere: Four season variability and solar effects on the layer bottomside at McMurdo (77.8°S, 166.7°E), Antarctica, *J. Geophys. Res.*, *117*, D22303, doi:10.1029/2012JD018079.

Zhang, F., C. A. Davis, M. L. Kaplan, and S. E. Koch (2001), Wavelet analysis and the governing dynamics of a large-amplitude mesoscale gravity-wave event along the East Coast of the United States, *Q. J. R. Meteorol. Soc.*, *127*(577), 2209–2245, doi:10.1002/qj.49712757702.

Zink, F., and R. A. Vincent (2001a), Wavelet analysis of stratospheric gravity wave packets over Macquarie Island: 1. Wave parameters, *J. Geophys. Res.*, *106*(D10), 10,275–10,288, doi:10.1029/2000JD900847.

Zink, F., and R. A. Vincent (2001b), Wavelet analysis of stratospheric gravity wave packets over Macquarie Island: 2. Intermittency and mean-flow accelerations, *J. Geophys. Res.*, *106*(D10), 10,289–10,297, doi:10.1029/2000JD900846.